NASA CONTRACTOR REPORT 165853

A STUDY OF MODEL DEFLECTION MEASUREMENT TECHNIQUES APPLICABLE WITHIN THE NATIONAL TRANSONIC FACILITY

B. P. HILDEBRAND, AND
J. L. DOTY

SPECTRON DEVELOPMENT LABORATORIES, INC.
COSTA MESA, CALIFORNIA 92626

CONTRACT NAS1-16564
FEBRUARY, 1982

National Aeronautics and
Space Administration

Langley Research Center
Hampton, Virginia 23665

NASA CONTRACTOR REPORT 165853

A STUDY OF MODEL DEFLECTION MEASUREMENT TECHNIQUES APPLICABLE WITHIN THE NATIONAL TRANSONIC FACILITY

B. P. HILDEBRAND, AND
J. L. DOTY

SPECTRON DEVELOPMENT LABORATORIES, INC.
COSTA MESA, CALIFORNIA 92626

CONTRACT NAS1-16564
FEBRUARY, 1982

National Aeronautics and
Space Administration

Langley Research Center
Hampton, Virginia 23665

N83-13075#

TABLE OF CONTENTS

NO. PAGE

TABLE OF CONTENTS. i

LIST OF FIGURES. iii

1.0 INTRODUCTION 1

2.0 GENERAL OPTICAL CONSIDERATIONS 6

- 2.1 Model Surface Characteristics 6
- 2.2 Ambient Refractive Index Variations 7
- 2.3 Local Refractive Index Variations 9

3.0 MOIRÉ CONTOUR ANALYSIS 15

- 3.1 Basic Moiré Contouring. 15
- 3.2 Projection Moiré for Remote Sensing 18
  - 3.2.1 Fringe Projection. 22
  - 3.2.2 Standard Projection Moiré Contouring . . . 29
  - 3.2.3 Differential Projection Moiré Contouring. 45
  - 3.2.4 Moiré Within the NTF 48

4.0 SCANNING HETERODYNE INTERFEROMETRY 51

- 4.1 The Basic SHI System. 51
  - 4.1.1 Beam Alignment 53
  - 4.1.2 Signal Detection and Deflection Measurement. 56
  - 4.1.3 Step Response and Bandwidth. 61
- 4.2 Optical Homodyne and Heterodyne Detection 63
- 4.3 Phase Locked Loop Detection 66

TABLE OF CONTENTS (Continued)

NO. PAGE

4.4 Laboratory Experiments. 68

5.0 CONTOUR HOLOGRAPHY 73

5.1 Basic Holographic Recording and Reconstruction. 73

5.2 Multiple Wavelength Contour Holography. 79

5.3 Contour Holography Within the NTF 85

6.0 SUMMARY CONCLUSIONS AND RECOMMENDATIONS. 92

REFERENCES 96

LIST OF FIGURES

NO. PAGE

1 The NTF Test Section and Plenum. 2

2 The Windows for Optical Access to the Test Section . . . 5

3 The Index of Refraction Perturbations About an NACA 64A010 Airfoil With a 2.36 cm (6 inch) Chord: $M_\infty = 0.8$; $M_c = 2 \times 10^6$ 10

4 The Vertical Measurement Error That Would Occur as a Result of Assuming No Local Index Perturbations. 13

5 The Geometry of Basic Moiré Contouring 16

6 A System for Projection Moiré Contouring 19

7 The Optics of Fringe Projection. 23

8 Diffraction Effects in a Focused Spot. 26

9 The Relationship Between the Model Coordinate Space (x,y,z) and the Image Coordinate Spaces of the Projection Arm (a',b',c') and the Observation Arm (α',β',γ') 28

10 The Shadows Cast by the Projection Arm 32

11 The Shadows that Appear to be Cast by the Observation Arm. 33

12 The Planar Sum and Difference Fringes of the TELECENTRIC Configuration. 35

13 The Location of the Hyperbolic Sum Fringes for Nontelecentric Moiré 37

14 The Limiting Cases of the Hyperbolic Sum Fringes 38

15 The Coordinate Space Variation of the Hyperbolic Sum Fringes with Variable Fringe Order (N) 39

16 An Approximation to the Hyperbolic Sum Fringes in the Immediate Neighborhood of the Model. 41

LIST OF FIGURES (Continued)

NO.		PAGE
17	The Variation of the Major and Minor Axes of the Elliptical Difference Fringes as Functions of the Fringe Order Parameter μ	42
18	The Location of the Elliptical Difference Fringes in the Neighborhood of the Model	44
19	A Two-Wavelength Scanning Heterodyne Interferometry System	52
20	Signal Amplitude as a Function of Beam Misalignment. . .	54
21	Scanning Heterodyne Interferometry with a Modulated Source	57
22	Model Surface Step Input	62
23	The Power Spectral Density of the Received Optical Heterodyne Signal.	65
24	The Configuration of the Limited Scale Scanning Heterodyne Interferometry Mock-Up.	69
25	The Frequency Variation of the SHI Mock-Up with Changing Target Distance R	71
26	Recording and Reconstruction of a Simple Hologram. . . .	74
27	The Basic Geometries for Recording a Hologram of a Diffuse Object	76
28	Recording and Reconstruction Geometry and Notation . . .	78
29	The Contour Fringes Generated by 2 Wavelength Holographic Contouring	82
30	The Relative Positions of the Observed Image Points. . .	84
31	A Possible Configuration for 2 Wavelength Holographic Contouring Within the NTF.	87

1.0 INTRODUCTION

The purpose of this investigation was to establish specific performance requirements and goals for a model deflection sensor to be installed in the National Transonic Facility (NTF) presently under construction at NASA's Langley Research Center. The system as envisioned will be nonintrusive, and have the capability of mapping or contouring the surface of a 1 x 1 meter model with a resolution of 50 to 100 points. It is anticipated that the surface to be measured will be located within ±0.5 meter of the centerline of the tunnel. The ultimate purpose of the model deflection sensor is to measure a maximum deformation of 7.62 cm (3 inches) with an accuracy of ± 64 μm (±0.0025 inch). These requirements are summarized in Table 1.

Three distinct concepts - moiré contouring, scanning interferometry and holographic contouring - were examined in detail for their practicality and potential to meet the above requirements. A review of the literature was conducted and extended by theoretical analysis to determine the capabilities and limitations of each concept within the constraints set by the geometry of the NTF test section. Because of the contractor's extensive practical experience with both holography and moiré systems, it was determined that experimentation in those areas at this time would unnecessarily dilute the effort. Hence, laboratory work was limited to the scanning interferometry approach where it was felt that the additional insight gained would be advantageous.

Of major importance throughout this program were practical considerations of the test section geometry and environment. Figure 1 is a simplified cross-sectional illustration of the NTF test section and plenum.

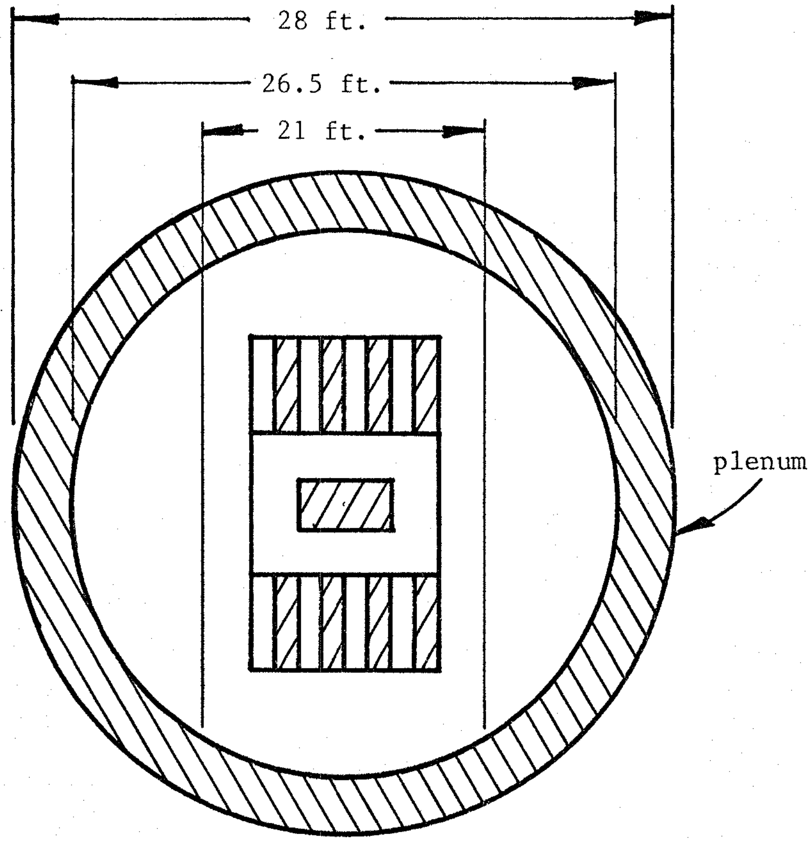

tunnel 2.13 m (7 ft.) wide

2.44 m (8 ft.) high

FIGURE 1. The NTF Test Section and Plenum

TABLE 1

Measurement Area	1 x 1 meter
Transverse Resolution	50 - 100 points
Measurement Range	1 meter
Maximum Deflection	7.62 cm (3 inches)
Measurement Accuracy	± 64 μm (0.0025 inch)

The tunnel itself is approximately 2.13 m (7 ft.) wide by 2.44 m (8 ft.) high. The ceiling and floor of the tunnel are supported by hollow "wall beam assemblies" within which room is available for installation of equipment. For a model deflection sensor, optical access is provided between the inside of a "wall beam assembly" and the tunnel interior by a series of 12.7 cm (5 inch) fused silica windows. Figure 2 illustrates the window pattern that will exist in both the floor and ceiling of the tunnel.

The space available behind each window within the "wall beam assembly" is approximately 61 cm (24 in.) x 79 cm (31 in.) x 14 cm (5½ in). Additionally, there is an as yet partially undefined area at the bottom of the plenum where it may be possible to install peripheral equipment. Any equipment installed within the plenum, however, will have to operate properly over a temperature range of -196° C to +71° C, and in pressures as high as 8.8 atmospheres. Obviously, if this necessitates the use of heavily insulated, thermally controlled packaging, space constraints become even more critical.

The results of this program provide a solid understanding of the limitations of each of the three techniques as they apply within the geometry of the NTF. Specifically, moiré contouring, while workable, is limited in its accuracy by the large depth of focus required (1 meter). On the other hand, scanning interferometry has the potential of enormous versatility, but again, without advancing the state of the art, cannot provide sufficient measurement accuracy. Holographic contouring, however, would be relatively simple to apply, and would, at the same time, yield a full field of data with readily defined contours.

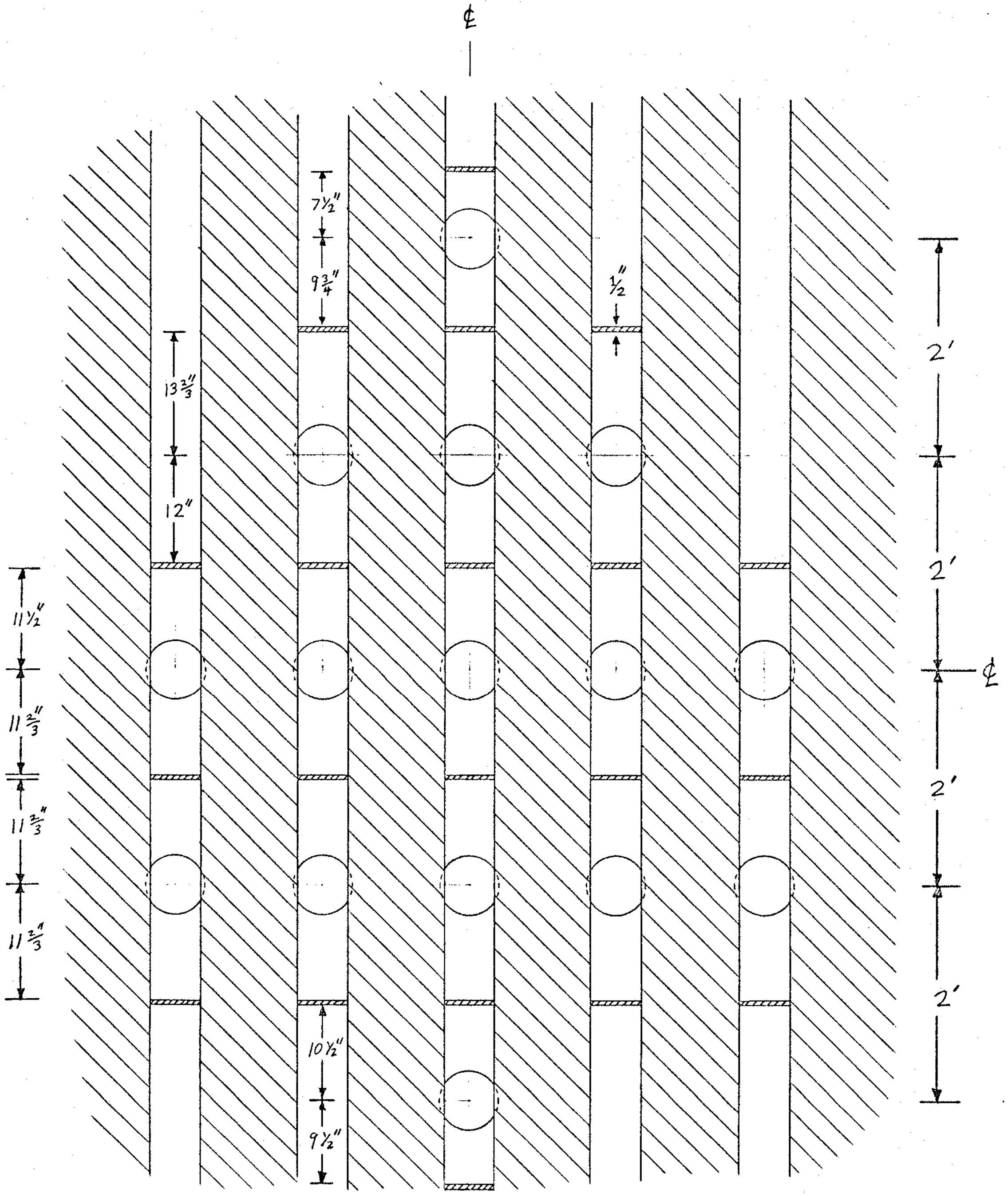

FIGURE 2. The Windows for Optical Access to the Test Section

2.0 GENERAL OPTICAL CONSIDERATIONS

There are certain phenomena which must be considered in a system of this nature that are inherent to the use of optical radiation. The effect of such phenomena upon model deflection measurements, be it deleterious or not, will be, to a large extent, characteristic of the radiation and independent of the technique employed.

This chapter examines the most important of these phenomena and the extent to which they will affect model deflection measurements. Also considered, though specific solutions to these difficulties are not within the scope of this contract, are methods that may be employed to minimize, correct, or nullify any adverse effects that arise.

2.1 Model Surface Characteristics

For optical sensing, the ideal model surface would be a diffuse Lambertian scatterer with a high surface reflectivity and low absorption. As a practical rule, the reflection characteristics of a surface are highly specular if the surface has an RMS roughness of $\lambda/4$ or less, where λ is the wavelength of the radiation employed ($\lambda \cong 0.5$ µm). Commonly, to achieve a properly diffuse characteristic, the surface is roughened considerably beyond this[1]. This is at odds, however, with the extreme surface smoothness (0.25 µm) required to minimize the conditions that trigger aerodynamic boundary layer separation at transonic velocities.

One possible solution to this dilemma is to go ahead and roughen the surface to achieve the desired optically diffuse characteristic. The surface would then be treated by coating it with a thin, hard, and as yet undefined substance that is both mechanically smooth and optically transparent. The result would be an outer surface that is sufficiently smooth to minimize boundary layer separation, yet is transparent and will pass the optical radiation to the diffusely scattering surface below. Of course, the surface that is optically sensed will be different from the surface of aerodynamic effect. And if the thickness of the coating is such that this difference is significant, it will have to be accounted for.

Ultimately, if a solution to this dilemma cannot be found, it will either place an upper limit on the flow conditions in which the model deflection sensor may be employed, or it will necessitate a system capable of detecting optical radiation over an extremely wide dynamic range. Note that since the required surface finish is on the order of $\lambda/2$, it can be expected to exhibit some diffuse scattering, though the effect will be minimal. It may, however, be sufficient to make a wide dynamic range system viable if care is taken to insure that the surface is not overpolished. Of course, the requirement for a wide optical dynamic range strongly limits the choice of methods for sensing the optical radiation, and precludes the use of such devices as video monitors.

2.2 Ambient Refractive Index Variations

As the temperature, pressure, and composition of the gas flowing within the tunnel is altered, so too will be its refractive index, and hence, its optical path length (L_o), which is the parameter that any optical system actually measures. The optical path length is

$$L_o = nL \tag{10}$$

where n is the refractive index of the medium through which the light passes, and L is the true path length.

The index of refraction of a gas varies according to the relationship

$$n = 1 + K\rho \tag{2}$$

where K is the Gladstone-Dale constant (for air $K = 2.25 \times 10^{-4} \frac{m^3}{Kg}$) and ρ is the density of the gas. Ignoring changes in composition and using this relationship, and the ideal gas law

$$\rho = \frac{P}{RT} \tag{3}$$

where P is the pressure, T is the temperature, and R is a constant of proportionality, Table 2 lists the extreme variations in refractive index that may be encountered within the NTF test section.

TABLE 2

$P(\frac{Kg}{m^2})$	$T(°K)$	$\rho(\frac{Kg}{m^3})$	n
5.02×10^4	344	1.06	1.000239
4.44×10^5	77	42.0	1.009450

Note that the variation in index of refraction is 0.92%. If ambient index variations are ignored this would result in an absolute measurement error of 9.2 mm over a path length of 1 meter, or a differential measurement error of 0.7 mm at the specified maximum deflection of 7.6 cm. Hence, to achieve the desired accuracy of ±64 µm, the ambient (free stream) index of refraction will have to be monitored and recorded for proper data reduction.

2.3 Local Refractive Index Variations

It is well known that the aerodynamic forces in the immediate vicinity of the model produce density, and hence, refractive index gradients on or about the model surface. This fact is used to advantage in many flow field studies where light is employed to probe the test section. Such an optical probe yields data on the index field, which can then be related to the density field through Equation 2. However, for model deflection measurements, such index variations are decidedly disadvantageous since they perturb the measurement in a possibly unpredictable fashion.

Consider Figure 3, which is a photograph of the reconstruction of a holographic interferogram recorded by the contractor in an earlier study[2] in the NASA/Ames 2' x 2' Transonic tunnel. During these tests the tunnel conditions were maintained at a free stream Mach number of 0.8 and a chord Reynolds number of 2×10^6. The model was an instrumented NACA 64A010 airfoil with a 2.36 cm (6 inch) chord. It was supported at both ends by transparent fused silica windows, and a collimated beam of laser radiation was passed through the flow field parallel to its span.

The flow field is essentially two dimensional and visible as a series of fringes, each of which corresponds to a shift in the optical path length of λ. Choosing the span as the z axis, the general form of Equation 1 is

$$L_o(x,y) = \int_{z_1}^{z_2} n(x,y)dz \quad . \tag{4}$$

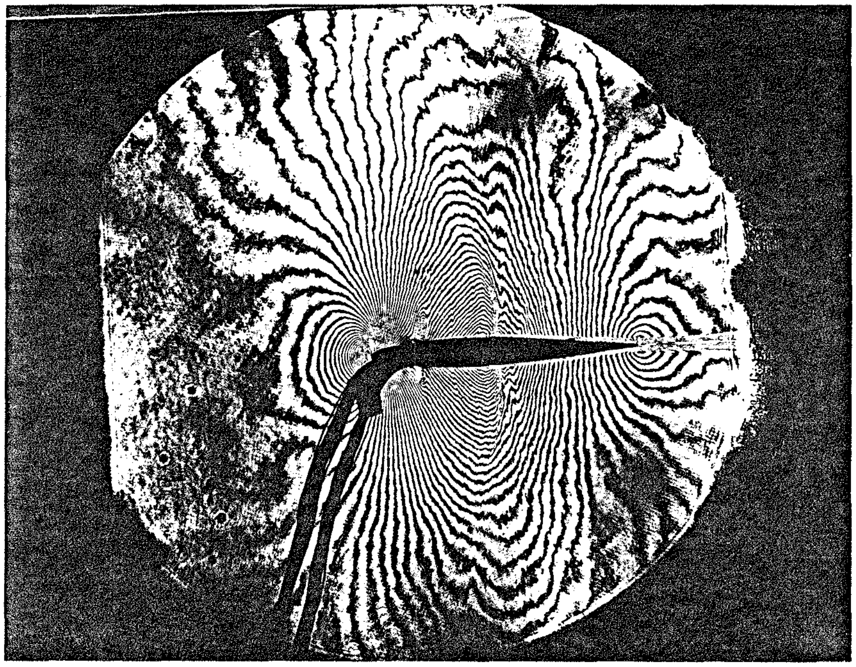

FIGURE 3. The Index of Refraction Perturbations About an NACA 64A010 Airfoil With a 2.36 cm (6 inch) Chord: $M_\infty = 0.8$; $M_c = 2 \times 10^6$

And since in Figure 3 the flow field is two dimensional,

$$L_o(x,y) = (z_2-z_1)n(x,y) = Ln(x,y) \tag{5}$$

where in this case L is the span of the wing. Next, by counting fringes from a relatively undisturbed point in the flow field, and assigning the number N to each fringe, the local index of refraction of any fringe can be related to the free stream index of refraction (n_∞) by the following equation:

$$L[n(x,y)-n_\infty] = \lambda N(x,y) \tag{6}$$

or

$$n(x,y) = n_\infty + \frac{\lambda}{L} N(x,y) \tag{7}$$

where N(x,y) is the two dimensional fringe number field, and N = 0 corresponds to the free stream (n_∞) condition.

Using this procedure, the two dimensional index distribution of Figure 3 can be obtained. Next, to determine its effect on a model deflection sensor which would probe from above, the optical path length along the x axis is determined by the relationship

$$H_o = \int_{x_1}^{x_2} n(x,y)\,dx \tag{8}$$

$$= (x_2-x_1)n_\infty + \frac{\lambda}{L}\int_{x_1}^{x_2} N(x,y)\,dx \quad . \tag{9}$$

Now the purpose of the probe is to measure the true path length (H) which is $\left(x_2-x_1\right)$ in Equation 9. The quantity that is actually measured is H_o, the optical path length. If the assumption is made that there are no local index variations, and H is computed from the simple relationship

$$H = \frac{H_o}{n_\infty} \qquad (10)$$

to account for the ambient index of refraction, the error that results is

$$\Delta H = \frac{H_o}{n_\infty} - (x_2 - x_1)$$

$$= \frac{\lambda}{L n_\infty} \int_{x_1}^{x_2} N(x,y)dx \quad . \qquad (11)$$

Using this procedure and the data of Figure 3, ΔH was computed at several points along the chord of the wing and the results are presented in Figure 4.

Note that the maximum extent of the measurement error (-2.5 μm) would be far less than the required measurement accuracy listed in Table 1 (±64 μm), and could therefore be ignored without significant effect. This is a result of the fact that the optical probe for deflection measurement samples from above, traversing the flow field in a direction that is, for the most part, perpendicular to isoindex surfaces, minimizing its path length through index extremes.

For the case of vertically oriented surfaces, however, it is likely that portions of the optical probe will traverse parallel to, and within index extremes. But this merely corresponds to the original situation of Figure 3, where the data was recorded by a collimated beam of light traversing the flow field parallel to the span of the wing. Here, the maximum error that would occur as a result of assuming no local index variations is +32.6 μm, which is still within the required measurement accuracy. Furthermore, this is an extreme example in which a single ray of light

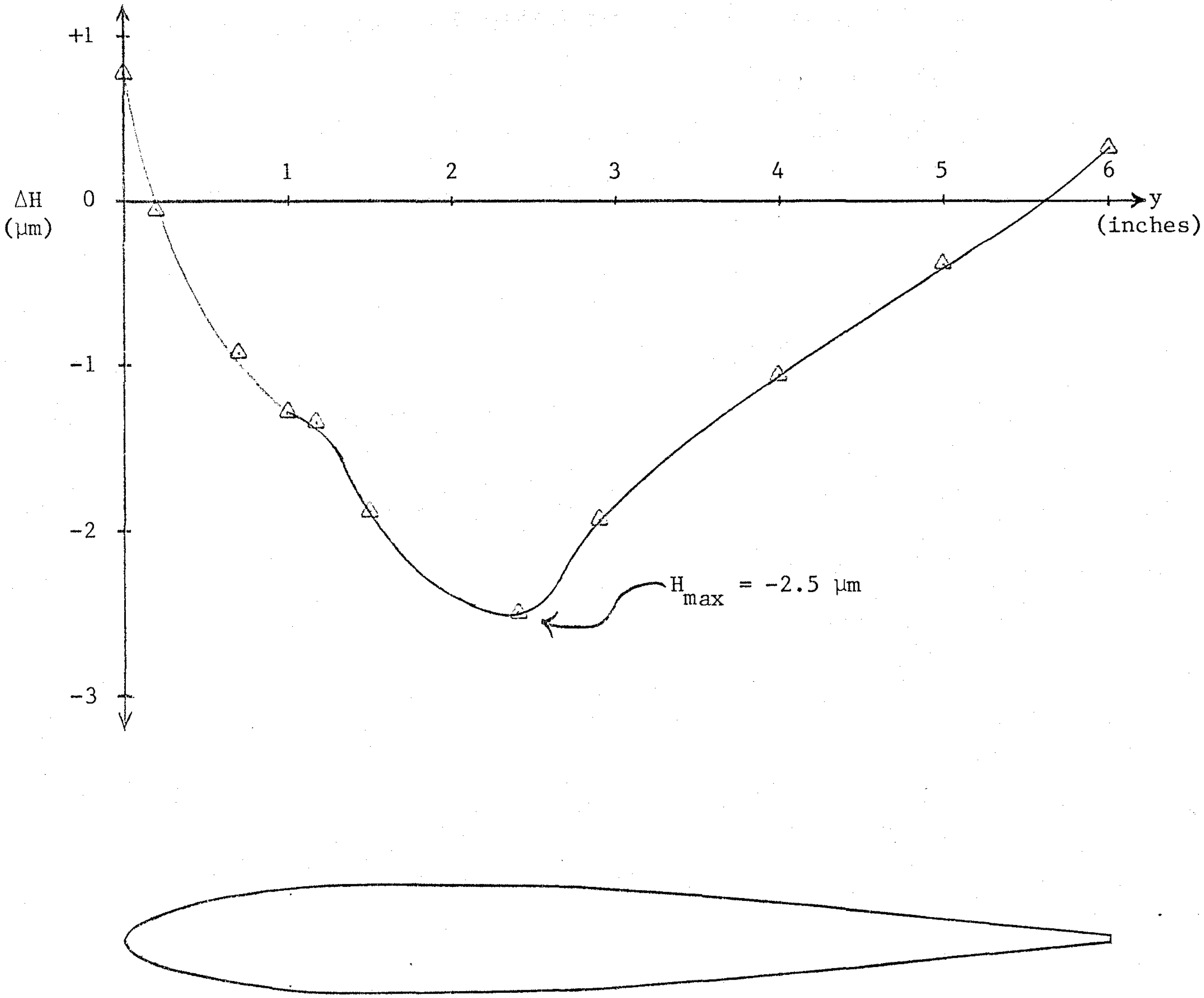

FIGURE 4. The Vertical Measurement Error That Would Occur as a Result of Assuming No Local Index Perturbations.

propagates parallel to the model surface for a distance of 61 cm (2 feet), an unlikely circumstance.

As stated earlier these computations were based on data taken in the Ames 2' x 2' Transonic tunnel. Obviously, the environmental extremes anticipated within the NTF test section will influence these results. But since the conditions in the two tunnels are similar (transonic), and the geometry is of the same order, it is felt that these results are a good indication of how local index perturbations will affect model deflection measurements.

3.0 MOIRÉ CONTOUR ANALYSIS

The phenomenon of moiré fringes was first described by Lord Rayleigh in 1874[3]. He noted that when two matched line gratings were placed in contact "... in such a manner that the lines are nearly parallel ..." an additional series of wide parallel bars developed with characteristics that were a function of the line spacing and inclination. The moiré phenomenon was little used until recently because of the difficulties encountered in the manufacture and reproduction of satisfactory gratings. However, in the early 1950's a novel technique was developed[4] whereby diffraction gratings could be reliably reproduced from a turned master grating, and the field has since blossomed into a powerful metrological technique.

This chapter describes the basic moiré technique and its extension to the geometry of the NTF test section. The important relationships and parameters are derived for projection moiré, which is an extension of the basic principle for application to remote, noncontact, noninvasive sensing. Also considered is the technique of differential moiré, in which the differential motion of the object surface may be isolated from surface shape data.

3.1 Basic Moiré Contouring

The application of basic moiré contouring was first reported in 1970 by Meadows, Johnson and Allen[5]. Their technique was a near-contact method in which the shadow of a grid was cast directly onto the object surface, as illustrated in Figure 5. The source of illumination was a collimated beam of incoherent radiation. The grating spacing was large enough,

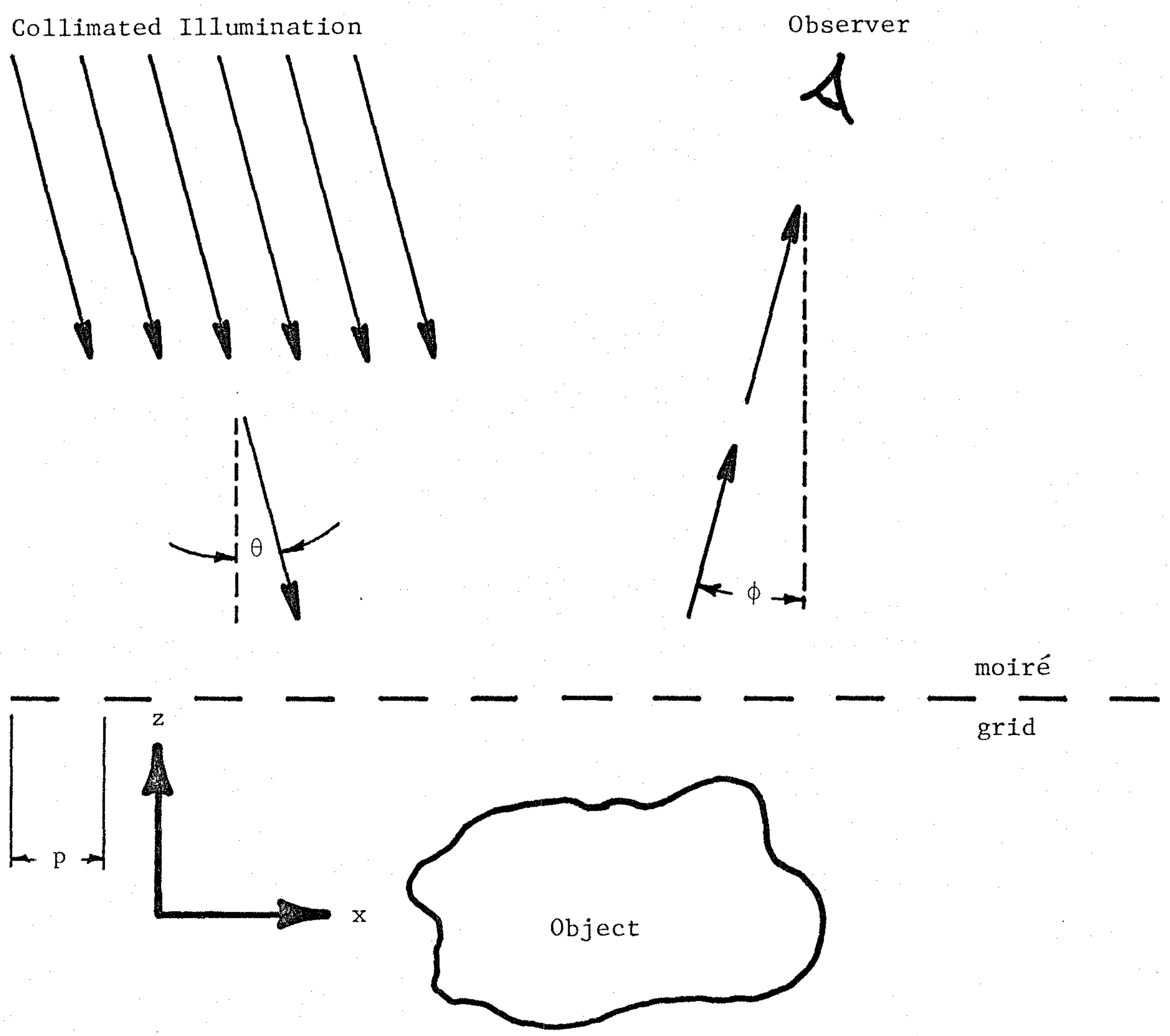

FIGURE 5. The Geometry of Basic Moiré Contouring

and its distance from the object small enough, so that diffraction effects in the projected shadow were negligible. The object was viewed through the same grating used to cast the shadow fringe pattern, and the observer was located far enough from the grid so that the lines of sight from the observer to the grid were essentially parallel for all points on the grid.

The result of such a configuration is that the object appears to have not only the grid shadows, but a series of additional shadows (moiré fringes) which represent the intersection of equally spaced contour planes with the surface of the object. The contour planes are literally a separate spatial frequency generated by beating the spatial frequency of the illumination grid with that of the observation grid. In this case both grids are one and the same, and the contours are planes that are parallel to the plane of the grid (the x-y plane) and have a spacing of

$$\Delta z = \frac{p}{\tan\theta + \tan\phi} \qquad (12)$$

where d is the grid spacing, and θ and ϕ are the illumination and observation angles as illustrated in Figure 5. If the contour spacing (Δz) is much greater than the grid spacing (p), then the moiré contours are easily separable from the grid shadows.

This form of basic moiré contouring is extremely powerful under the right circumstances. However, it has certain drawbacks which make it impractical in the NTF. Namely, the grid must be located relatively close to the object to prevent deleterious diffraction effects. Obviously, placing a grid close to the model in a transonic wind tunnel is impossible. And while the grid spacing can be widened, which will allow it to be removed from the immediate vicinity of the model, this necessitates an increase in the contour spacing and, therefore, a reduction in measurement accuracy. Even then, the grid, as well as the window through which its shadow is cast, must be as large as the model if full coverage is desired. It is these difficulties that necessitate a modification of the basic moiré technique.

3.2 Projection Moiré for Remote Sensing

The optical configuration of a projection moiré system is illustrated in Figure 6. It consists mainly of a projection and an observation arm which respectively project and view moiré shadow fringes on the model. The model is centered on the origin of an x,y,z Cartesian coordinate system. Note that the x axis is perpendicular to the plane of the figure. Both the projection and observation arms have optic axes that lie in the y,z plane; intersect the origin; and are removed from one another by an angle 2θ. Note that the z axis bisects this angle, and that there is no loss of generality here since unequal projection and observation angles can be represented by a simple rotational transformation of the model coordinate space. The system operates in the following fashion:

> An incoherent, white light source illuminates the grating in the projection arm, which is in turn imaged onto the model surface. Now while the grating itself is two dimensional, and has no significant longitudinal depth, its image has a longitudinal depth that is equal the depth of focus of the imaging optics, which is chosen to be equal to the maximum depth of the model. Hence, the image of the projection grating in the vicinity of the model consists of dark and light planes which can be, but are not necessarily, parallel to one another. These planes are illustrated by the shaded

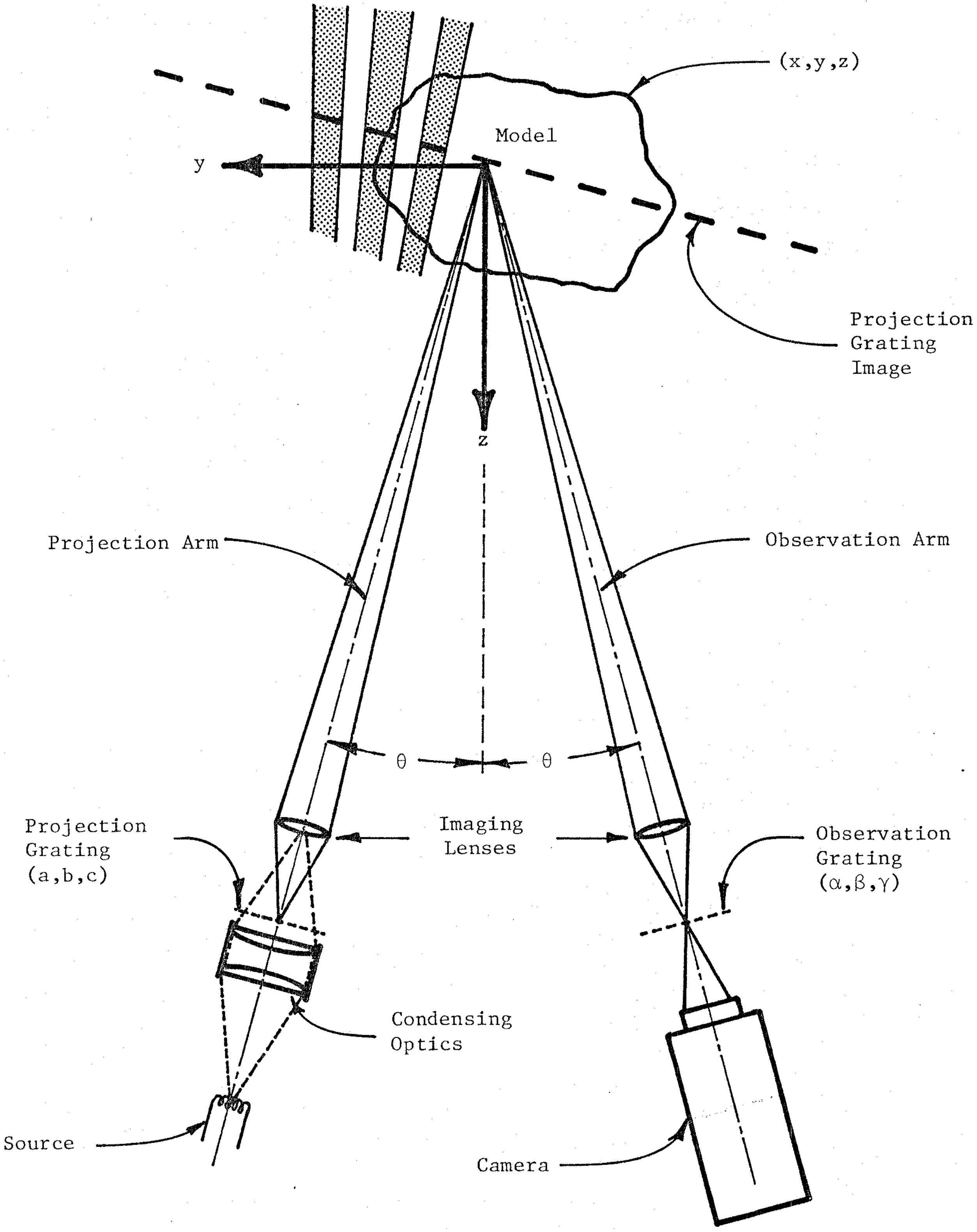

FIGURE 6. A System for Projection Moiré Contouring

bands in the model space of Figure 6. Note that for clarity of the illustration, only some of the grating lines have been shaded in this fashion.

If the transmission function of the projection grating is defined as $T_p(a,b,c)$, where a,b,c is the Cartesian coordinate space of the projection grating, and if it is illuminated by the uniform intensity I_s, then the intensity seen by the imaging lens is

$$I_p(a,b,c) = I_s T_p(a,b,c) \quad . \tag{13}$$

The intensity distribution projected into the model coordinate space is

$$I_p(x,y,z) = I_s T_p(x,y,z) \tag{14}$$

where $I_p(a,b,c) \rightrightarrows I_p(x,y,z)$ (15)

represents the imaging transformation from the projection grating to the model coordinate space. At the model, the intensity of the light scattered to the observer is

$$R(x,y,z) = S(x,y,z) I_p(x,y,z) \tag{16}$$

where $S(x,y,z)$ is the localized point scattering function of the surface of the model, assumed to be diffuse and Lambertain.

Now the imaging lens of the observation arm collects and images this scattered light onto the observation grating. The intensity distribution of this image before passing through the observation grating is $R(\alpha,\beta,\gamma)$ where α,β,γ is the Cartesian coordinate space of the observation grating, and

$$R(x,y,z) \rightrightarrows R(\alpha,\beta,\gamma) \tag{17}$$

represents the imaging transformation from the model to the grating coordinate space. If the intensity transmission function of the observation grating is defined as $T_o(\alpha,\beta,\gamma)$, then the intensity distribution seen by the observer is

$$I_o(\alpha,\beta,\gamma) = T_o(\alpha,\beta,\gamma)R(\alpha,\beta,\gamma) \quad . \tag{18}$$

And since the imaging transformation of a properly corrected imaging lens is linear, the transformation of Equation 16 is merely,

$$R(\alpha,\beta,\gamma) = S(\alpha,\beta,\gamma)\ I_p(\alpha,\beta,\gamma) \quad . \tag{19}$$

Therefore, it follows from Equations 14, 15, 18 and 19 that

$$I_o(\alpha,\beta,\gamma) = I_s\ S(\alpha,\beta,\gamma)\ T_o(\alpha,\beta,\gamma)\ T_p(\alpha,\beta,\gamma) \quad . \tag{20}$$

To interpret Equation 20, which represents the observed image, note that $I_s\ S(\alpha,\beta,\gamma)$ is merely the image that would be recorded if both gratings were removed so that

$$T_o = T_p = 1 \quad . \tag{21}$$

However, with the gratings in the system, the intensity distribution of the model image is modulated by the combined transmission function

$$T(\alpha,\beta,\gamma) = T_o(\alpha,\beta,\gamma)\ T_p(\alpha,\beta,\gamma) \quad . \tag{22}$$

The moiré fringes are beat spatial frequencies that arise as a result of the multiplication on the right hand side of Equation 22.

To understand fully the manner in which this occurs, it will be necessary to consider some specific grating transmission functions. However, when doing so, it will be more instructive if the observed intensity distribution in Equation 20 is referred to the coordinate space of the model. This merely requires the reverse of the imaging transformation in Equation 17, which is itself an imaging transformation from the observation grating to the model coordinate space. And again, since such a transformation is linear,

$$I_o(x,y,z) = I_s\ S(x,y,z)\ T(x,y,z) \tag{23}$$

where $T(x,y,z) = T_o(x,y,z)\ T_p(x,y,z) \quad .$

Note that because of the simple transformations involved, the moiré phenomenon is equivalent to projecting the shadows of both gratings onto the surface of the model in such a way that the resultant intensity is the product of the two projection intensities, rather the sum, as would be the actual case. This is perhaps the simplest way of understanding and analyzing the moiré phenomenon, and it is the method used throughout this program.

3.2.1 Fringe Projection

The optical configuration for projecting the shadow of a grating onto the model surface is illustrated in Figure 7. For clarity, the illumination source and condensing optics have not been included, and the projection lens is modeled as a simple lens with a remote aperture, which is accurate for a well corrected system.

The illumination is incident from the left. It strikes the grating, which acts as a transmission filter, then passes through the aperture to the lens. The aperture is included to limit the cone of rays accepted by the lens from any point on the grating, and hence, it is the system STOP. The lens takes the cone of rays from a point on the grating, and redirects it to a point in the image. The object and image positions (L and L') are related to one another through

$$\frac{1}{L} + \frac{1}{L'} = \frac{1}{F} \tag{24}$$

where F is the focal length of the lens. The magnification of the system (m) is defined as the ratio of the image to the object height which is

$$m = \frac{L'}{L} \quad . \tag{25}$$

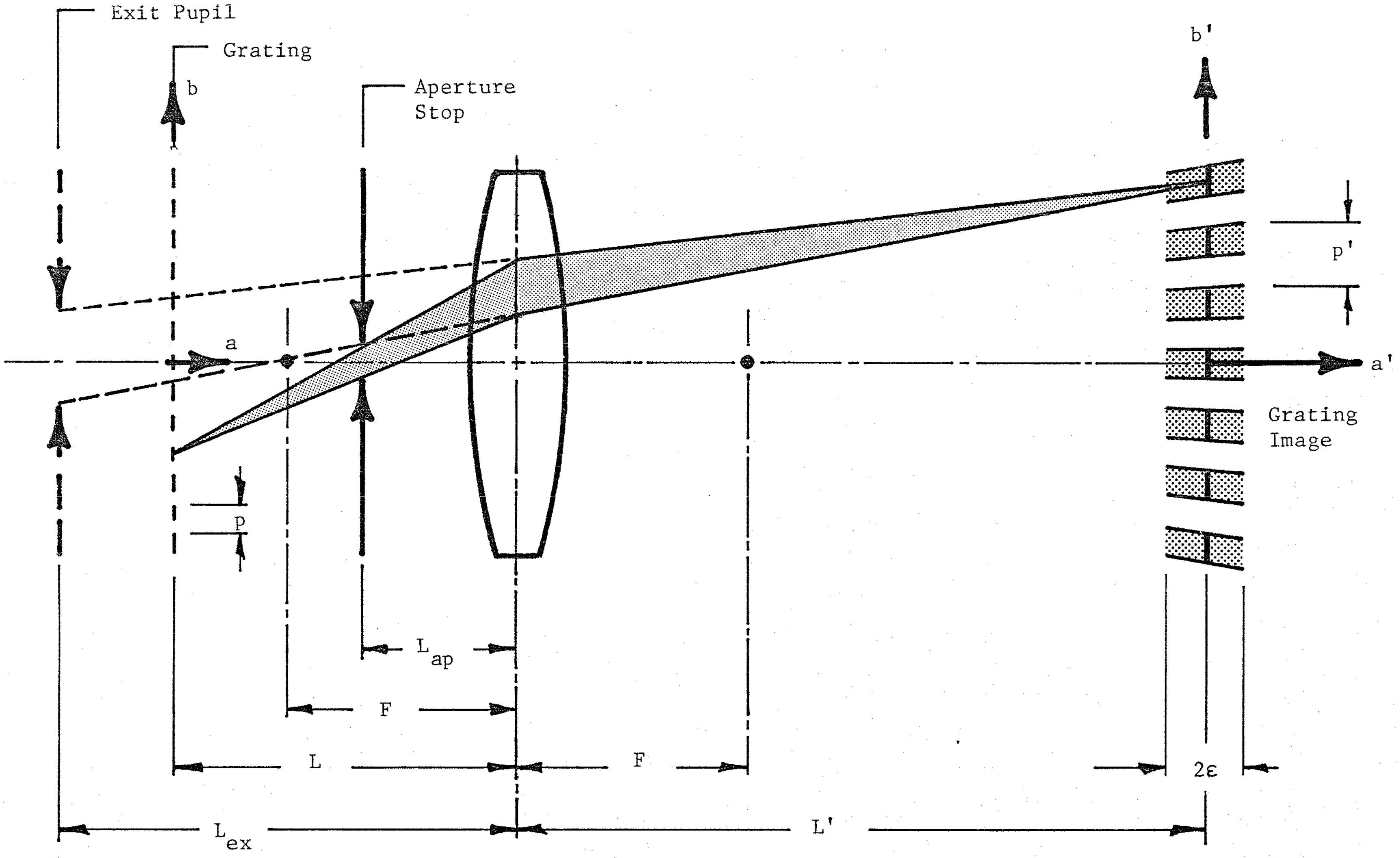

FIGURE 7. The Optics of Fringe Projection

Therefore, if the grating has a line spacing of p, then its image has a line spacing of p', where

$$p' = mp \quad . \tag{26}$$

Now the cone of rays that forms any point on the image appears to come from an aperture that is the virtual image of the aperture stop, and is referred to as the exit pupil. The position of the aperture stop and exit pupil are related through

$$\frac{1}{L_{ap}} - \frac{1}{L_{ex}} = \frac{1}{F} \tag{27}$$

which is a modified form of the imaging relationship in Equation 24.

Equations 24 through 27 are a result of the classic imaging relationships that are derived and discussed in any number of references, a few of which are given here[6,7,8].

Now consider a sinusoidal transmission grating with a transmission function

$$T_p(a,b,c) = \frac{1}{2}\,[1+\cos(2\pi\frac{b}{p})] \tag{28}$$

where p is the line spacing of the grating, and a,b,c is its Cartesian coordinate space as defined in Figure 7. The image of this grating is a fan of planar shadows in the a',b',c' coordinate space (also defined in Figure 7) that intersect at the center of the exit pupil. The imaging transformation yields

$$T_p(a',b',c') = \frac{1}{2}\left\{1+\cos\left[\frac{2\pi}{p'}\,L_p(a',b')\right]\right\} ; \quad |a'| \leq \varepsilon \tag{29}$$

where $$L_p(a',b') = \frac{(L'+L_{ex})b'}{L'+L_{ex}+a'} \tag{30}$$

and ε is the depth of focus of the optical system, which determines the longitudinal depth of the planar shadows.

At this point it will be instructive to digress and discuss the diffraction effects encountered here. Figure 8 illustrates the diffraction phenomenon that occurs at a focused spot. Instead of focusing to an infinitesimal spot as geometric rays predict (the large dashed lines in Figure 8), the light diffracts outward to form a large central disc enclosed in a series of concentric rings[6,7]. This pattern is named the Airy distribution after the man who first derived it, and the bright central disc is referred to as the Airy disc.

The Airy disc contains 83.8% of the incident energy, and has a diameter of

$$D_s = 2.44\lambda \frac{L'}{D_L} \tag{31}$$

where λ is the wavelength of light; L' and D_L are defined in Figures 7 and 8. Two such spots can just be distinguished from one another when their centers are separated by half the diameter of the Airy disc (Equation 31). Any closer, and it becomes difficult to resolve them as separate spots because they blur together and appear as one. Hence, $D_s/2$ is considered the resolution limit of an optical system.

The depth of focus is here defined as the longitudinal range over which the geometric ray spot is less than or equal to the Airy disc. Therefore, considering similar triangles in Figure 8,

$$\frac{D_L}{L'} = \frac{D_s}{\varepsilon} \tag{32}$$

or, rearranging

$$\begin{aligned} \varepsilon &= D_s \frac{L'}{D_L} \\ &= 2.44\lambda \left(\frac{L'}{D_L}\right)^2 \quad . \end{aligned} \tag{33}$$

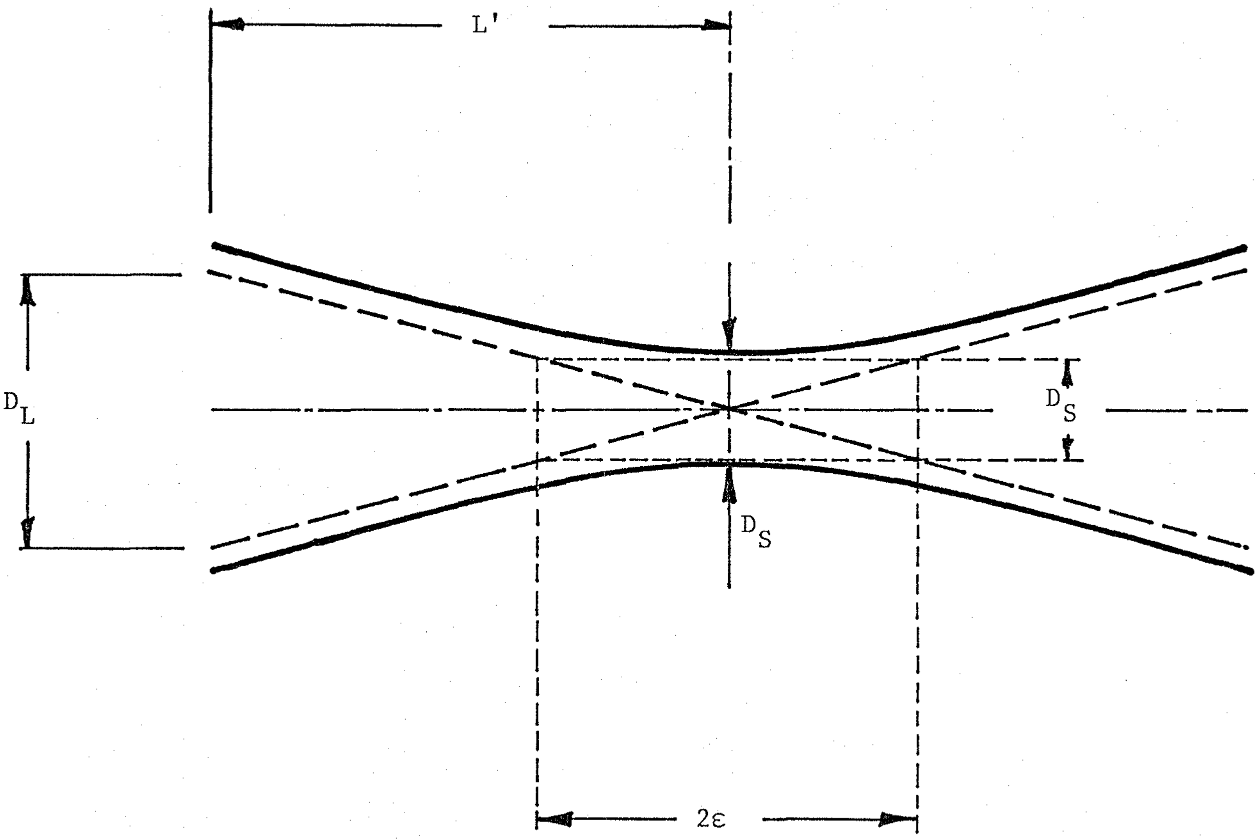

FIGURE 8. Diffraction Effects in a Focused Spot

$\pm\varepsilon$ is the range over which the grating shadows are in focus in the image space of Figure 7. Furthermore, to insure that two adjacent shadow planes in the grating image can be resolved one from the other, the condition

$$p' \geq D_s \tag{34}$$

is imposed on the system.

Returning to the projected transmission function of Equations 29 and 30, a rotational transformation is required to relate it to the x,y,z coordinate space of the model. Figure 9 illustrates the relationship between the model coordinate space and the image coordinate spaces of the projection arm (a',b',c') and the observation arm (α',β',γ'). To transform the transmission function of Equations 29 and 30, the following direct substitution is made:

$$\left.\begin{aligned} a' &= -z\cos\theta - y\sin\theta \\ b' &= +y\cos\theta - z\sin\theta \quad . \end{aligned}\right\} \tag{35}$$

Hence,

$$T_p(x,y,z) = \frac{1}{2}\left\{1+\cos\left[\frac{2\pi}{p'}\,L_p(y,z)\right]\right\} \tag{36}$$

where $$L_p(y,z) = \frac{(L'+L_{ex})(y\cos\theta - z\,\mathrm{son}\theta)}{L'+L_{ex} - z\cos\theta - y\sin\theta} \tag{37}$$

As before, the above shadow distribution is in focus only within the depth of focus (ε), and hence, subject to the condition

$$|a'| \leq \varepsilon \quad . \tag{38}$$

The projected shadow planes of Equations 36-38 are illustrated in Figure 10.

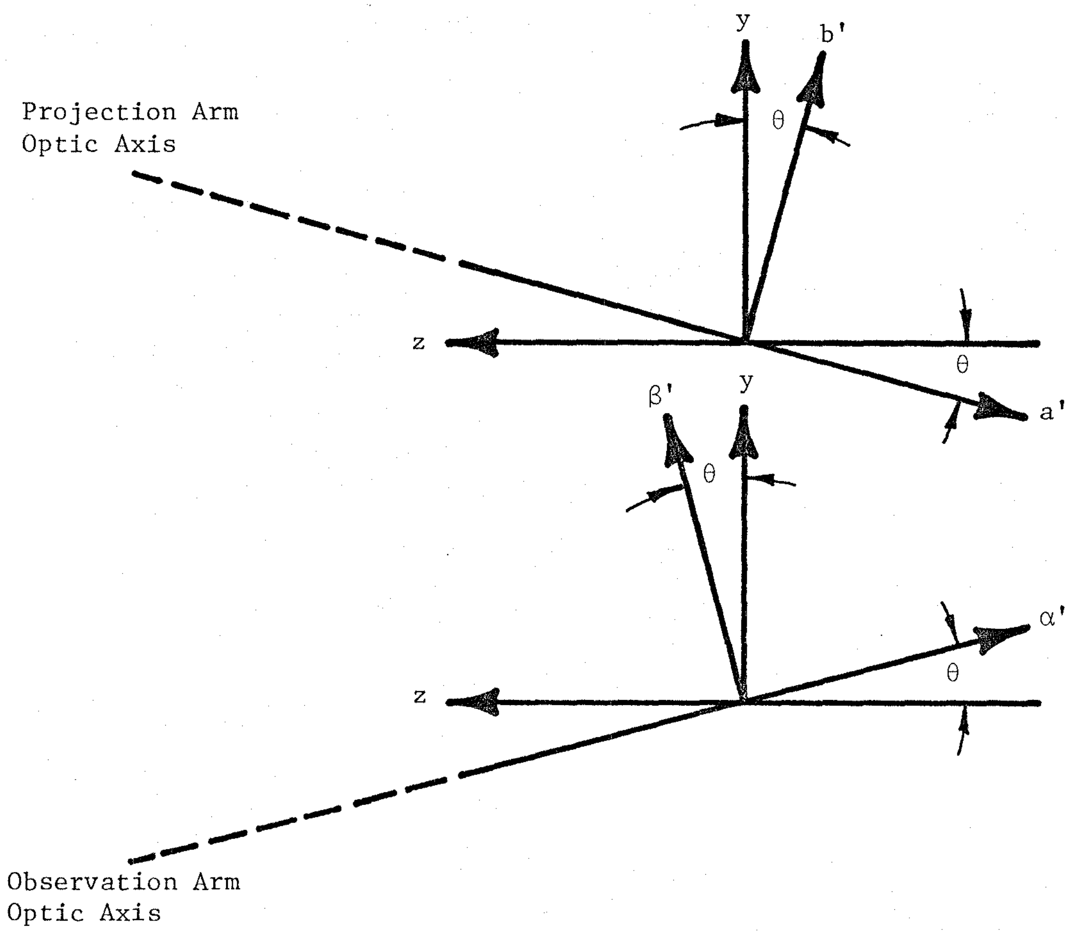

FIGURE 9. The Relationship Between the Model Coordinate Space (x,y,z) and the Image Coordinate Spaces of the Projection Arm (a','b'c') and the Observation Arm (α',β',γ').

3.2.2 Standard Projection Moiré Contouring

In standard projection moiré contouring the object is to generate a contour map of the surface of the model. To do so, a straight line grating with a transmission function like that of Equation 28 is used in both the projection and observation arm of the system. Note that most practical gratings exhibit a square wave transmission function as opposed to the sinusoidal distribution considered here. The sinusoidal analysis is, however, simpler, and has been shown to yield the same result as to contour location and spacing[5].

The projected shadow distribution of the projection arm is taken to be

$$T_p(x,y,z) = \frac{1}{2}\left\{1+\cos\left[\frac{2\pi}{p'} L_p(y,z)\right]\right\} \tag{39}$$

where $$L_p(y,z) = \frac{d_p(y\cos\theta - z\sin\theta)}{d_p - z\cos\theta - y\sin\theta} \tag{40}$$

which is identical to Equations 36 and 37 but with the distance from the model to the exit pupil $(L'+L_{ex})$ replaced by the variable d_p for simplicity. As stated before, the observation arm can be looked upon as also casting shadow planes in an identical fashion to that of Section 3.2.1. But the grating coordinate space of the observation arm corresponding to Figure 7 is α, β, γ, rather than a, b, c, and the grating image space is α', β', γ', rather than a',b',c'. The purpose for this distinction is illustrated in Figure 9, where the final rotational transformation from the α', β', γ' space to the x,y,z space is carried out using Equation 35, but with θ replaced by $-\theta$. Hence, the projected shadow distribution of the observation arm is

$$T_o(x,y,z) = \frac{1}{2}\left\{1+\cos\left[\frac{2\pi}{o'}L_o(y,z)\right]\right\} \tag{41}$$

where $$L_o(y,z) = \frac{d_o(y\cos\theta + z\sin\theta)}{d_o - z\cos\theta + y\sin\theta}\ ; \tag{42}$$

o' is the magnified line spacing of the shadow planes; and d_o is the distance from the model to the exit pupil of the observation arm.

Inserting Equations 39 and 41 into Equation 23 yields

$$T(x,y,z) = \frac{1}{4}\left[1+\cos\left(\frac{2\pi}{p'}L_p\right)\right]\left[1+\cos\left(\frac{2\pi}{o'}L_o\right)\right] \tag{43}$$

and carrying out the multiplication

$$T(x,y,z) = \frac{1}{4}\left[1+\cos\left(\frac{2\pi}{p'}L_p\right)+\cos\left(\frac{2\pi}{o'}L_o\right)+\cos\left(\frac{2\pi}{p'}L_p\right)\cos\left(\frac{2\pi}{o'}L_o\right)\right] \tag{44}$$

The last term in Equation 44 can be expanded to yield

$$T(x,y,z) = \frac{1}{4}\left\{1+\cos\left(\frac{2\pi}{p'}L_p\right)+\cos\left(\frac{2\pi}{o'}L_o\right) + \frac{1}{2}\cos\left[2\pi\left(\frac{L_p}{p'} + \frac{L_o}{o'}\right)\right] + \frac{1}{2}\cos\left[2\pi\left(\frac{L_p}{p'} - \frac{L_o}{o'}\right)\right]\right\}. \tag{45}$$

Now, remembering that T(x,y,z) is the spatial modulation of the intensity distribution of the observed image, any term of the form

$$\cos[2\pi f(x,y,z)] \tag{46}$$

within T(x,y,z) describes a series of fringes whose location is determined by

$$f(x,y,z) = N \tag{47}$$

where N is any integer, and is here called the fringe number. Therefore, the intensity modulation function of Equation 45 produces four sets of fringes determined by

$$\frac{L_p}{p'} = N \tag{48}$$

$$\frac{L_o}{o'} = N \tag{49}$$

$$\frac{L_p}{p'} + \frac{L_o}{o'} = N \tag{50}$$

$$\frac{L_p}{p'} - \frac{L_o}{o'} = N \tag{51}$$

where L_p and L_o are defined in Equations 40 and 42.

Fringe Equation 48 represents the original shadow planes projected by the projection arm and illustrated in Figure 10. Fringe Equation 49 represents another set of shadow planes that appear to be projected onto the model surface, but in actuality exist only behind the grating in the observation arm. They are illustrated in Figure 11.

Fringe Equations 50 and 51 represent the sum and difference beat spatial frequencies of most interest here. To simplify their characteristics, the following approximations are made

$$\begin{aligned} d_p &= d_o = d \\ o' &= p' \end{aligned} \tag{52}$$

and with some manipulation, Equations 50 and 51 take on the form

$$\frac{y\cos\theta - z\sin\theta}{d - z\cos\theta - z\sin\theta} \pm \frac{y\cos\theta + z\sin\theta}{d - z\cos\theta + y\sin\theta} = \frac{Np'}{d} \tag{53}$$

where the + term represents the sum spatial frequencies (Equation 50) and the - term represents the difference spatial frequencies (Equation 51).

For contouring, the fringe shape is ideal if the aperture stop is located in the front focal plane of the projection lens in both arms of the system ($L_{ap} = F$ in Figure 7). This is the TELECENTRIC configuration, and its effect is to place the exit pupil at infinity, i.e.,

$$d = \infty. \tag{54}$$

Equation 53 then simplifies to

$$(y\cos\theta - z\sin\theta) \pm (y\cos\theta + z\sin\theta) = Np' \tag{55}$$

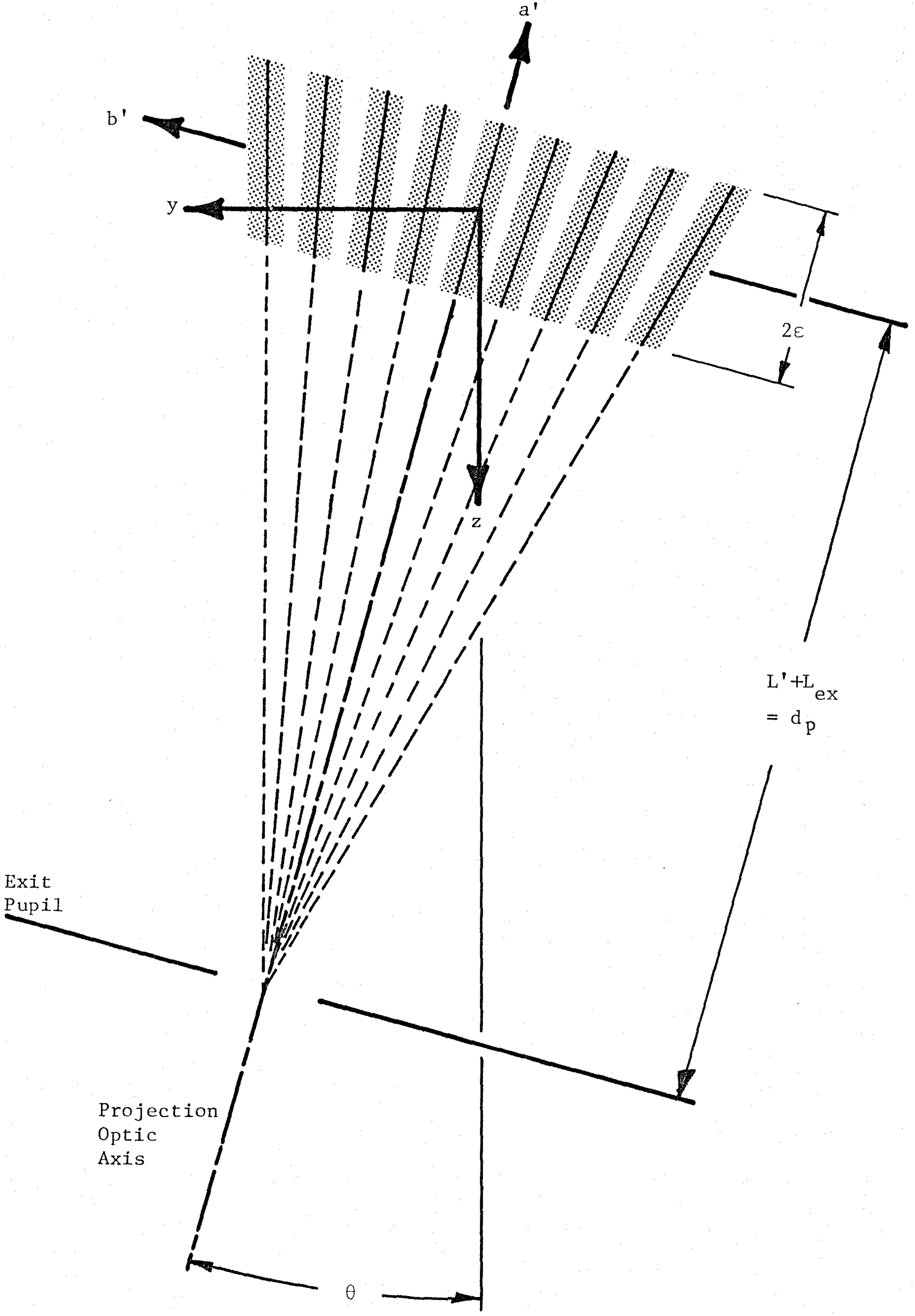

FIGURE 10. The Shadows Cast by the Projection Arm

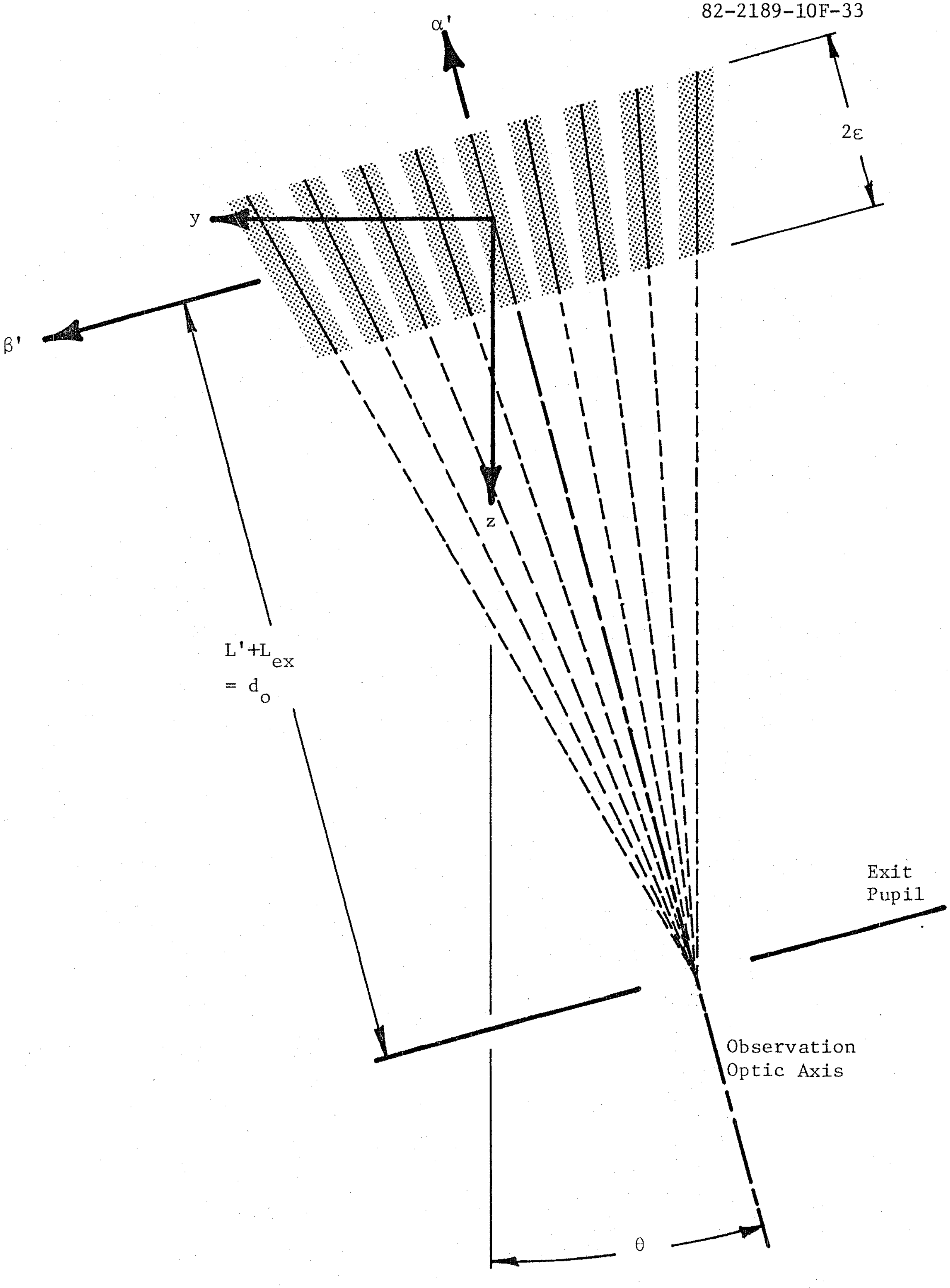

FIGURE 11. The Shadows that Appear to be Cast by the Observation Arm

which describes two sets of planar fringes in addition to those of the projection fringes of Figures 10 and 11. As illustrated in Figure 12, the sum fringes are parallel to the x,z plane with a spacing of

$$\Delta y = \frac{p'}{2\cos\theta} \quad , \tag{56}$$

and the difference fringes are parallel to the x,y plane with a spacing of

$$\Delta z = \frac{p'}{2\sin\theta} \quad . \tag{57}$$

If θ is small so that

$$\sin\theta << \cos\theta \tag{58}$$

then the sum fringes as well as the two sets of projection fringes all have a spacing of approximately p', while the spacing of the difference fringes is much greater. The difference fringes, therefore, appear as spatially separable contour planes parallel to the x,y plane of the model coordinate space.

Unfortunately, the telecentric configuration requires lenses and tunnel windows as large or larger than the model, which make it, like basic moiré, impractical within the NTF. For that reason, the more general case of a finite exit pupil location is considered next by dealing with Equation 53 without further simplification.

For the case of the sum fringes Equation 53, after further manipulation, yields

$$2y(d\cos\theta-z) = \frac{Np'}{d}\,[(d-z\cos\theta)^2-y^2\sin^2\theta] \quad . \tag{59}$$

There is no simple or convenient form for Equation 59. However, by expanding to the general form, and comparing with known cases, it is found that it represents a complex series of hyperbolas. Their locations are best understood by referring them to a y',z' coordinate space that

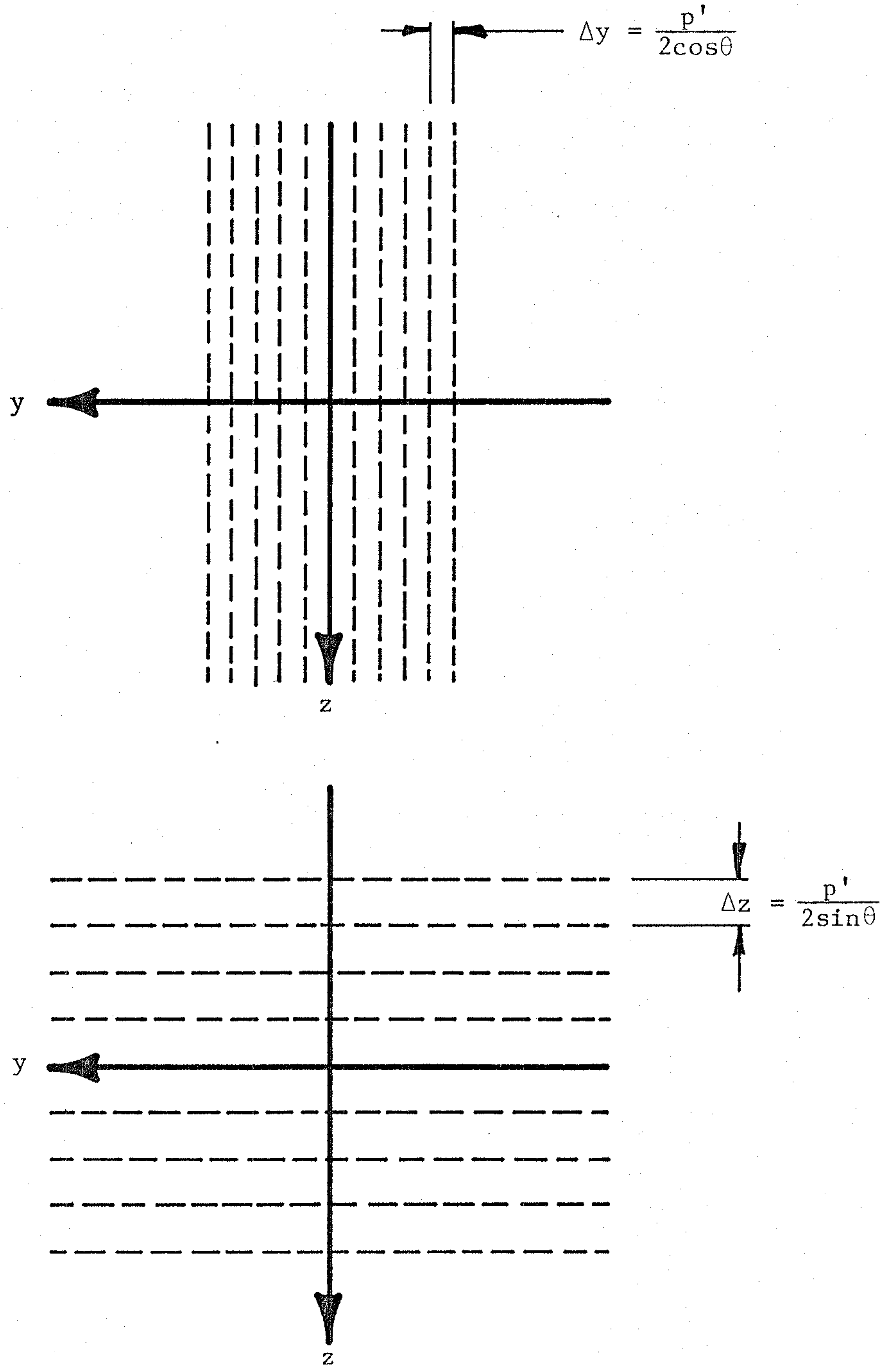

FIGURE 12. The Planar Sum and Difference Fringes of the TELECENTRIC Configuration

has an origin located at y_o, z_o in the y,z model space, and has been rotated through an angle η, as illustrated in Figure 13.

At N = 0, the two hyperbolas collapse to form two straight lines defined by the equations

$$\begin{aligned} y &= 0 \\ z &= d\cos\theta \quad . \end{aligned} \tag{60}$$

At N = ±∞ the two hyperbolas again collapse to form two straight lines defined by the equations

$$\begin{aligned} z &= \frac{d}{\cos\theta} + y\tan\theta \\ z &= \frac{d}{\cos\theta} - y\tan\theta \quad . \end{aligned} \tag{61}$$

Both of these situations are illustrated in Figure 14.

For N finite, the hyperbolas are as illustrated in Figure 15. Note that

1) the asymptotes of the hyperbolas of a given fringe order (N) are not perpendicular,
2) the locus of points of the origin of the y',z' system (x_o, y_o) traces out an ellipse in the y,z plane.
3) the y',z' coordinates rotate from -45° to +45° as N varies from $-\infty$ to $+\infty$.

Of primary importance, though, is the spacing of the fringes near the origin of the model space (y,z). Expanding Equation 59, and ignoring all second order terms, yields

$$y = \frac{Np'}{d}\left(\frac{d}{2\cos\theta} - z\right) \quad . \tag{62}$$

The sum fringes described by Equation 62 are a fan of planes, again with a spacing of

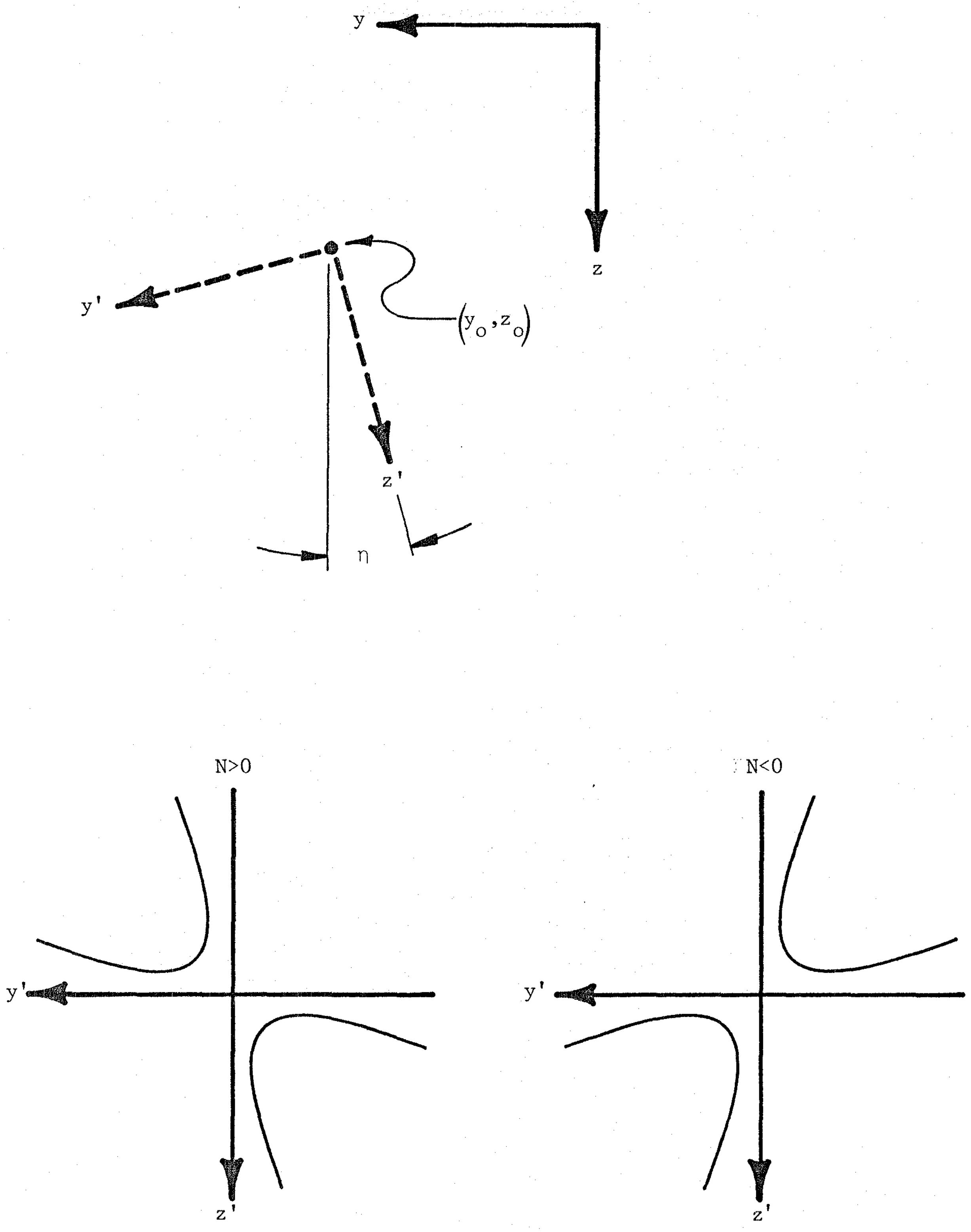

FIGURE 13. The Location of the Hyperbolic Sum Fringes for Nontelecentric Moiré

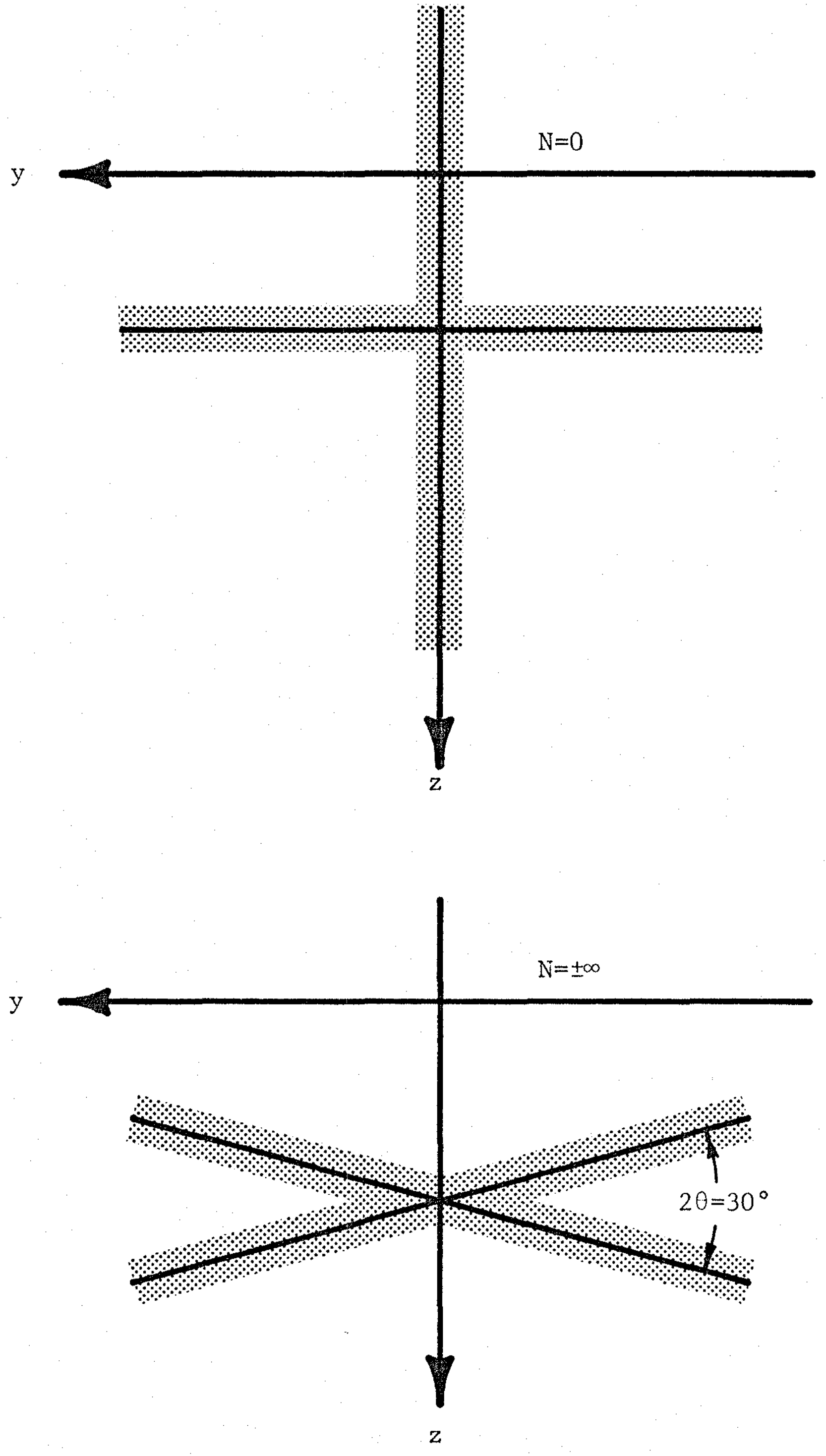

FIGURE 14. The Limiting Cases of the Hyperbolic Sum Fringes

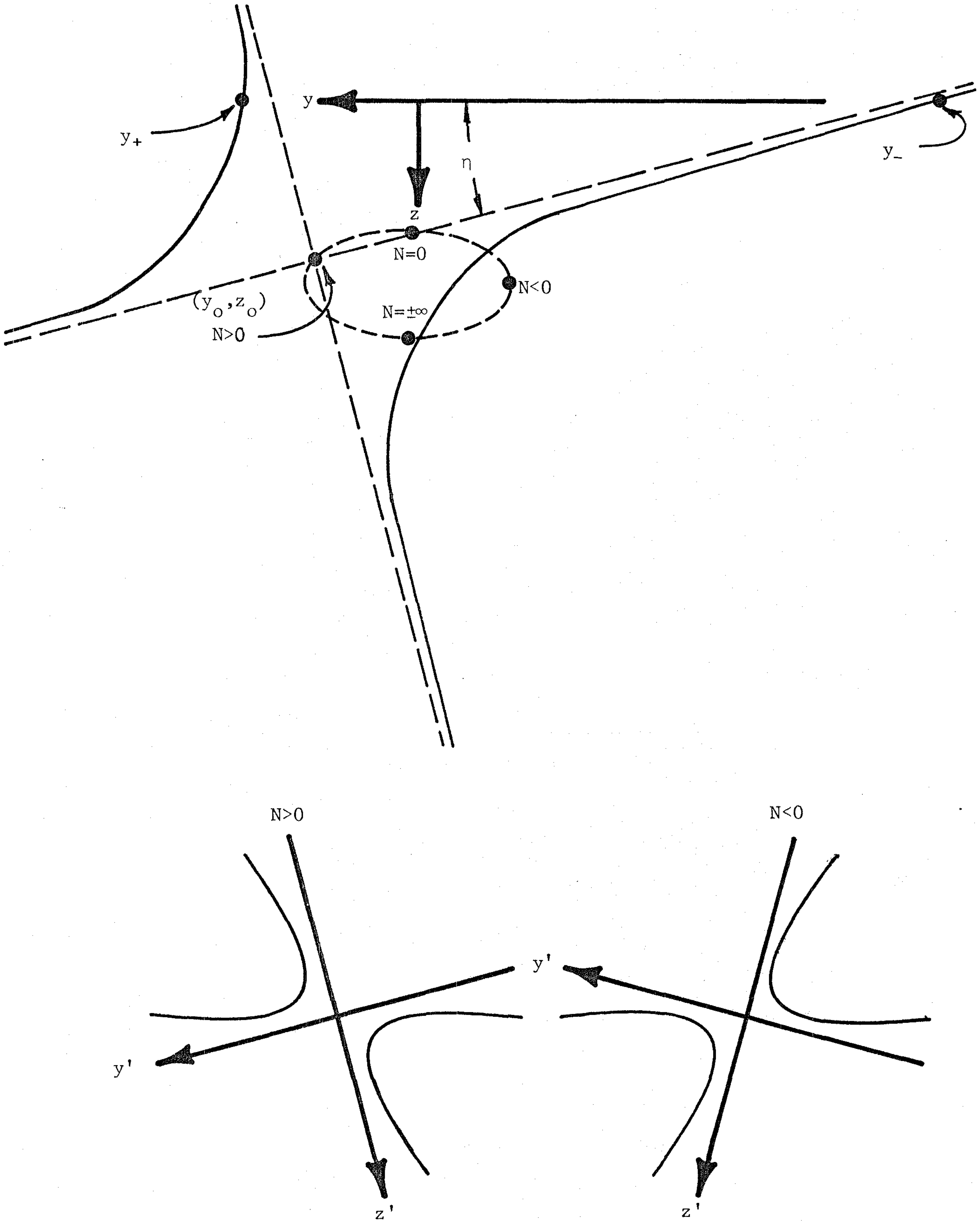

FIGURE 15. The Coordinate Space Variation of the Hyperbolic Sum Fringes with Variable Fringe Order (N)

$$\Delta y = \frac{p'}{2\cos\theta} \tag{63}$$

but no longer parallel to the x,z plane. Rather, they appear to radiate from the coordinate

$$\begin{aligned} y &= 0 \\ z &= \frac{d}{2\cos\theta} \end{aligned} \tag{64}$$

as in Figure 16.

Next, for the case of the difference fringes, Equation 53, after rearranging, yields

$$2\sin\theta[y^2\cos\theta - z(d-z\cos\theta)] = \frac{Np'}{d}[(d-z\cos\theta)^2-(y\sin\theta)^2] \tag{65}$$

which, after further manipulation, becomes

$$\frac{(z-z_o^2)}{A^2} + \frac{y^2}{B^2} = 1 \tag{66}$$

where

$$z_o = \frac{d}{2\cos\theta}\left[\frac{1-\mu\cot\theta}{1-\frac{\mu}{2}\cot\theta}\right] \tag{67}$$

$$A^2 = \frac{\left(\frac{d}{2\cos\theta}\right)^2}{[1-\frac{\mu}{2}\cot\theta]^2} \tag{68}$$

$$B^2 = \frac{\left(\frac{d}{2\cos\theta}\right)^2}{[1-\frac{\mu}{2}\cot\theta][1+\frac{\mu}{2}\tan\theta]} \tag{69}$$

$$\mu = \frac{Np'}{d} \quad . \tag{70}$$

Figure 17 is a normalized graph of both A^2 and B^2 as functions of the fringe order parameter μ. Both have singularities at

$$\mu = -2\cot\theta \text{ and } +2\tan\theta \quad . \tag{71}$$

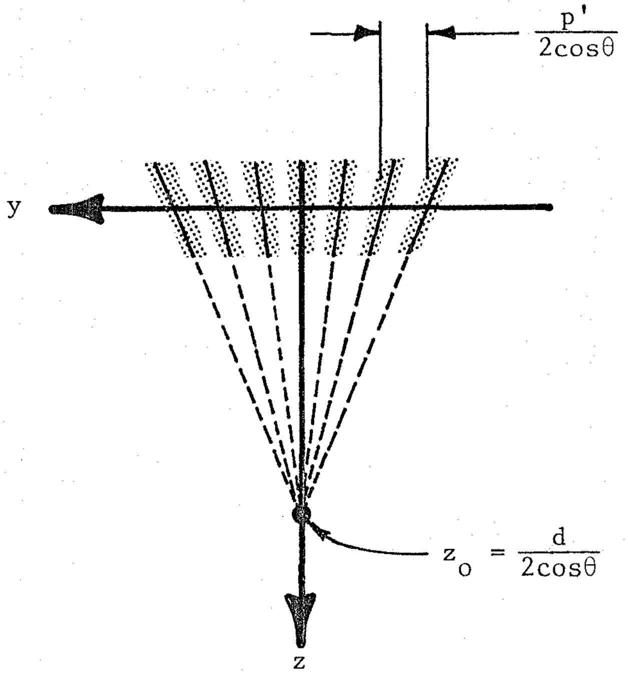

FIGURE 16. An Approximation to the Hyperbolic Sum Fringes in the Immediate Neighborhood of the Model

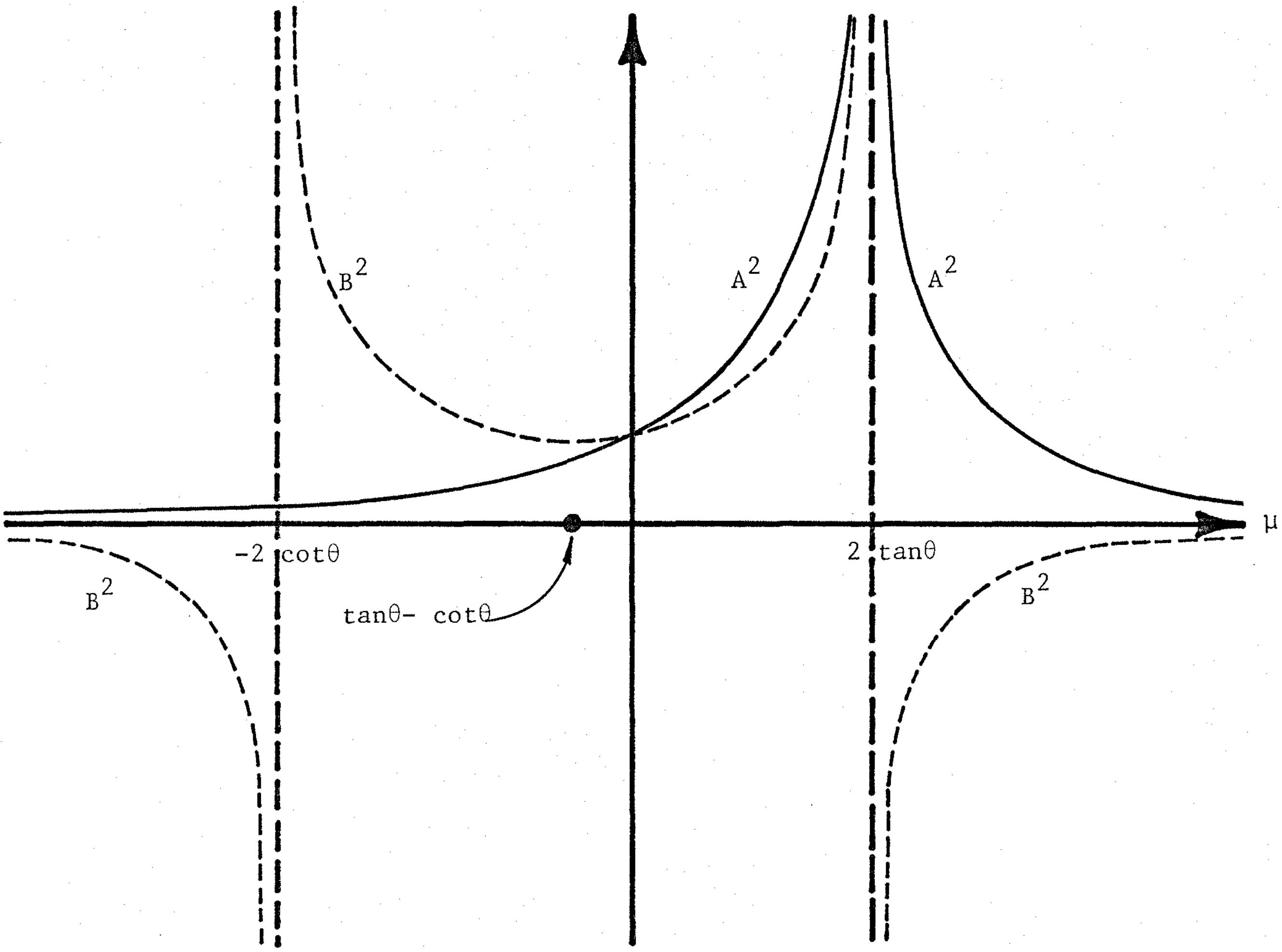

FIGURE 17. The Variation of the Major and Minor Axes of the Elliptical Difference Fringes as Functions of the Fringe Order Parameter μ.

But while A^2 is always positive, B^2 changes sign at both singularities. Hence, Equation 66 takes the form of a series of ellipses for B^2 positive,

$$-2\cot\theta < \mu < 2\tan\theta \quad , \tag{72}$$

and a series of hyperbolas for B^2 negative. Again, however, the fringes of most importance are those near the y,z origin where the model is located, which correspond to fringe order numbers near $N = 0$.

Figure 18 illustrates the location of the elliptical difference fringes for the range

$$\tan\theta - \cot\theta < \mu < 2\tan\theta \quad . \tag{73}$$

The lower limit in Equation 73 was chosen to be the value at which B^2 is a minimum. Note that as μ increases from the lower limit the fringes form expanding ellipses until the upper limit is reached, at which point they open out into a parabola. Beyond this they are again hyperbolas. Also note that

$$A^2 = B^2 \ @ \ \mu = 0 \quad . \tag{74}$$

Therefore, near the origin the fringes are nearly circular, with a spacing of

$$\Delta z = \frac{p'}{2\sin\theta} \quad . \tag{75}$$

The consequences, therefore, of a finite exit pupil location are:

1) the fringes are distorted from the simple planar shape, yielding a complex series of hyperbolas and ellipses that, in the neighborhood of the model, approximate a fan of extraneous planes and concentric, spherical contours;
2) the fringe spacing is variable with position, though in the limit as the origin is approached it is unchanged from the telecentric configuration.

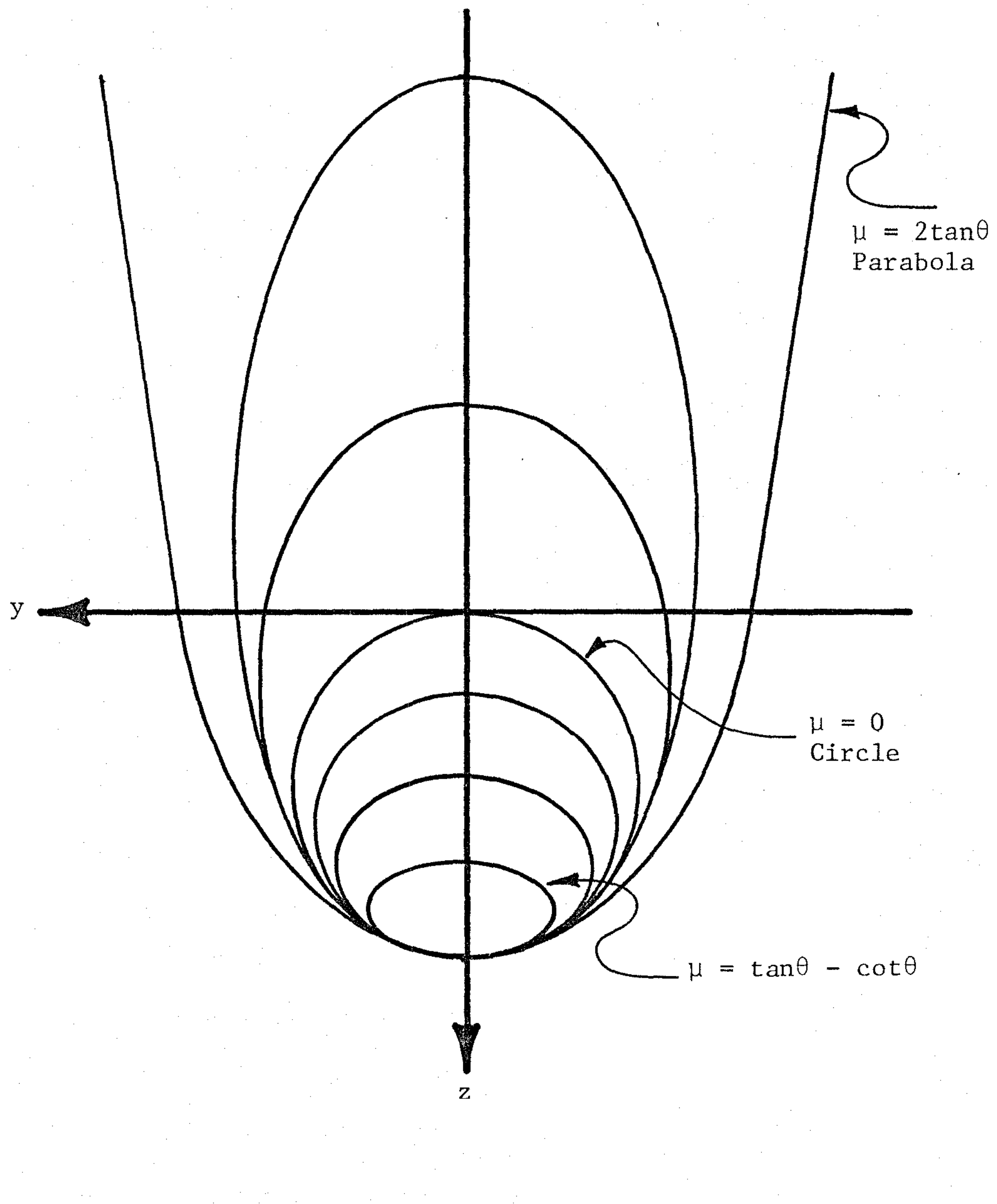

FIGURE 18. The Location of the Elliptical Difference Fringes in the Neighborhood of the Model

3.2.3 Differential Projection Moiré Contouring

The objective of differential moiré contouring is to isolate motion of the model surface from its shape. To do so the system of Figure 6 is used with a slight but significant modification. Namely, the simple line grating in the observation arm is replaced with a more complex grating that is representative of the model surface shape, and under the right circumstances the contour fringes that result are a function of model deflection alone.

To fabricate the observation grating for differential moiré, the simple observation grating for standard moiré is removed and replaced with unexposed film. The simple line grating is retained in the projection arm so that the film records a transparency of the projection grating fringes as they appear cast upon the model surface, but perturbed by the surface shape, position, and the angle of view of the observation arm. After processing, this transparency replaces the old observation grating in the otherwise unchanged system of Figure 6. The projection grating, still unchanged, projects fringes onto the model surface, which are again perturbed by the surface shape, position, and the angle of view of the observation arm. If the model surface is unchanged since the differential observation grating was recorded, then the observed perturbations match those in the differential observation grating through which they are viewed, and the difference spatial frequencies cancel. Hence, any difference frequencies present are a measure of change in the model surface shape and position.

As before, Equations 39 and 40 describe the fringes projected onto the model surface by the projection arm. During recording of the differential observation grating the model surface is described by the topographic function $z_o(x,y)$, and the optical intensity distribution at the film plane is

$$R_o(\alpha,\beta,\gamma) = I_s\, S_o(\alpha,\beta,\gamma)\, T_{po}(\alpha,\beta,\gamma) \tag{76}$$

where R, S and T_p are determined after the fashion of Equations 13-16, and

$$R(x,y,z_o) \rightleftarrows R_o(\alpha,\beta,\gamma) \tag{77}$$

represents the imaging transformation from the model coordinate space to that of the grating. Assuming an ideal film characteristic, the resultant transmission function of the developed film is

$$T_o(\alpha,\beta,\gamma) = R_o(\alpha,\beta,\gamma) \quad . \tag{78}$$

At a later time, with the developed film acting as the differential observation grating, the fringes cast by the projection arm are unchanged, but the model surface is assumed to have moved and/or warped to the new topographic function $z(x,y)$. As before, the intensity distribution scattered by the model is $R(x,y,z)$ which, after the imaging transformation becomes $R(\alpha,\beta,\gamma)$. This intensity distribution is filtered by the transmission characteristic of Equations 76-78 to yield the observed distribution

$$I_o(\alpha,\beta,\gamma) = R(\alpha,\beta,\gamma)\, R_o(\alpha,\beta,\gamma) \quad . \tag{79}$$

As before, it will be more instructive to relate the observed intensity distribution to the coordinate space of the model by reversing the imaging transformation. The result is

$$I_o(x,y,z) = I_s^2 S(x,y,z_o) S(x,y,z) T_p(x,y,z_o) T_p(x,y,z) \tag{80}$$

where z and z_o are both x and y dependent topographic functions. In this case Equations 39 and 40 apply for both transmission functions in Equation 80. And in a fashion similar to the derivation of Equation 45, the combined transmission function is

$$T(x,y,z) = 1/4\left\{1 + \cos\left(\frac{2\pi}{p'}L_p\right)+\cos\left(\frac{2\pi}{p'}L_o\right)+1/2\,\cos\left[\frac{2\pi}{p'}(L_p+L_o)\right] + 1/2\,\cos\left[\frac{2\pi}{p'}(L_p-L_o)\right]\right\} \quad (81)$$

where $L_p(y,z)$ is defined in Equation 40 and

$$L_o(y,z) = L_p(y,z_o) \quad . \quad (81a)$$

Again, there are four sets of fringes determined by

$$L_p = Np' \quad (82)$$

$$L_o = Np' \quad (83)$$

$$L_p+L_o = Np' \quad (84)$$

$$L_p-L_o = Np' \quad (85)$$

and as before, Equations 82 and 83 represent the original fringes projected on the model, while Equations 84 and 85 represent the sum and difference fringes. Making use of Equations 40 and 81, Equations 84 and 85 become

$$\frac{y\cos\theta-z\sin\theta}{d-z\cos\theta-y\sin\theta} \pm \frac{y\cos\theta-z_o\sin\theta}{d-z_o\cos\theta-y\sin\theta} = \frac{Np'}{d} \quad (86)$$

where d_p has been replaced by d. Of interest here are the difference spatial frequencies which, after manipulation of Equation 86, are determined by

$$(z-z_o)(y-d\sin\theta) = \frac{Np'}{d}[(d-y\sin\theta)^2-(d-y\sin\theta)(z+z_o)\cos\theta+zz_o\cos^2\theta] \quad . \quad (87)$$

The terms in Equation 87 have been grouped according to their z and z_o dependence. Note that the left side is a pure function of the difference between the two topographic surfaces z(x,y) and $z_o(x,y)$, whereas the right side is a function of their sum as well as their product. The contour fringes that result, therefore, are a complex function of both surface shape (z and z_o) as well as deflection ($z-z_o$). Only in the telecentric case (the limit as d approaches ∞) is the shape dependence removed, in which case Equation 87 reduces to

$$(z-z_o)\sin\theta = -Np' \quad . \tag{88}$$

But it was shown in Section 3.2.2 that a telecentric system is not practical in the NTF, and for that reason it is felt that in this program differential moiré offers no benefit in comparison to standard moiré.

3.2.4 Moiré Within the NTF

To design a standard moiré system for use in the NTF one must begin with the required depth of focus of the system as determined by Equation 33. Assuming the model has a potential depth about the centerline of the tunnel of ± 1/2 meter, then

$$\varepsilon = 0.5 \text{ m} \quad . \tag{89}$$

If visible radiation is used,

$$\lambda = 0.5 \text{ } \mu\text{m} \tag{90}$$

and inverting Equation 33

$$\frac{L'}{D_L} = \sqrt{\frac{\varepsilon}{2.44\lambda}} = 640 \quad . \tag{91}$$

Now the model is located at a distance of approximately 1.2 meter (4 ft.) from the tunnel windows. Hence,

$$L' = 1.2 \text{ meter} \tag{92}$$

and $$D_L = \frac{L'}{640} = 1.9 \text{ mm} \quad . \tag{93}$$

Therefore, the 7.6 cm windows installed in the test section are more than adequate. Now, from Equation 31 the diffraction spot size of such a system is

$$D_S = 2.44\lambda\left(\frac{L'}{D_L}\right) = 0.78 \text{ mm} \tag{94}$$

and the number of resolvable spots across the edge of a 1 meter square field of view is

$$N_S = \frac{1 \text{ meter}}{D_S} = 1281. \quad . \tag{95}$$

The transverse resolution is therefore more than sufficient. Now D_S also determines the minimum possible size for the projected fringe spacing, and therefore the greatest contouring accuracy. For that reason a grating spacing and projection magnification is chosen such that

$$p' = D_S \quad . \tag{96}$$

Finally, the locations of the windows place a limitation on the available choices for θ (see Figure 6). If two adjacent windows are used then (see Figure 2)

$$\theta = 9.4° \tag{97}$$

and from Equations 63, 75, 94, and 96, the extraneous sum fringes are spaced at

$$\Delta y = 0.40 \text{ mm} \tag{98}$$

with a contour spacing of

$$\Delta z = 2.4 \text{ mm} \quad . \tag{99}$$

Higher accuracy (reduced contour spacing) can be obtained by placing the projection and observation arms in widely separated windows. In that case

$$\left.\begin{aligned} \theta &= 34° \\ \Delta y &= .47 \text{ mm} \\ \Delta z &= .69 \text{ mm} \quad . \end{aligned}\right\} \tag{100}$$

Unfortunately, the spacing of the projected fringes (.78 mm) does not scale with θ, and the contours are no longer spatially separable because of near identical spatial frequencies. Allen and Meadows[9] have demonstrated a grid translation technique that removes the unwanted fringes by spatially translating both the observation and projection grid during a single frame cycle. Unfortunately, the relatively short exposure times required within the NTF make such a system an unlikely candidate for model deflection measurements.

It would also be possible to increase the accuracy by reducing the required depth of field in Equation 89. This would allow a wider aperture (D_L), a reduced spot size (D_S), and hence, a reduced projected fringe spacing (p'). But the square law relationship of Equation 91 requires a 100:1 reduction in the depth of field to obtain a 10:1 improvement in the contour spacing. That would mean that a system with a contour spacing of 0.24 mm would have a depth of field of 1 cm, an alternative that is not considered viable.

4.0 SCANNING HETERODYNE INTERFEROMETRY

Scanning heterodyne interferometry (SHI) is, in the sense that it samples one point at a time, a form of optical radar. But rather than measuring the time of flight of a pulse of radiation, it senses the phase of a continuous wave probe, and is therefore more akin to interferometry. Unfortunately, standard interferometry offers too great a sensitivity (typically 1/3 μm) to be applicable here. So to reduce the sensitivity to a more workable level, the probe in heterodyne interferometry consists of two optical signals at different frequencies that have been spatially superimposed, and it is the phase of the beat frequency of the returning signal that is sensed.

4.1 The Basic SHI System

Figure 19 illustrates a possible configuration for such a system. Two lasers operating at different frequencies are spatially mixed by the beamsplitter on the left. The resulting beam is split by a second beamsplitter, which allows a portion of the probe to be sampled immediately, providing a reference signal (S_r). The rest of the probe passes through a two-dimensional scanner where it is deflected to a point on the object. The scanner also samples a portion of the radiation scattered by the object and returns it via the original beam path to a second detector, yielding the probe signal (S_p). The radial distance from the scanner to the point on the object is obtained by a comparison of the relative phase of the two signals S_r and S_p.

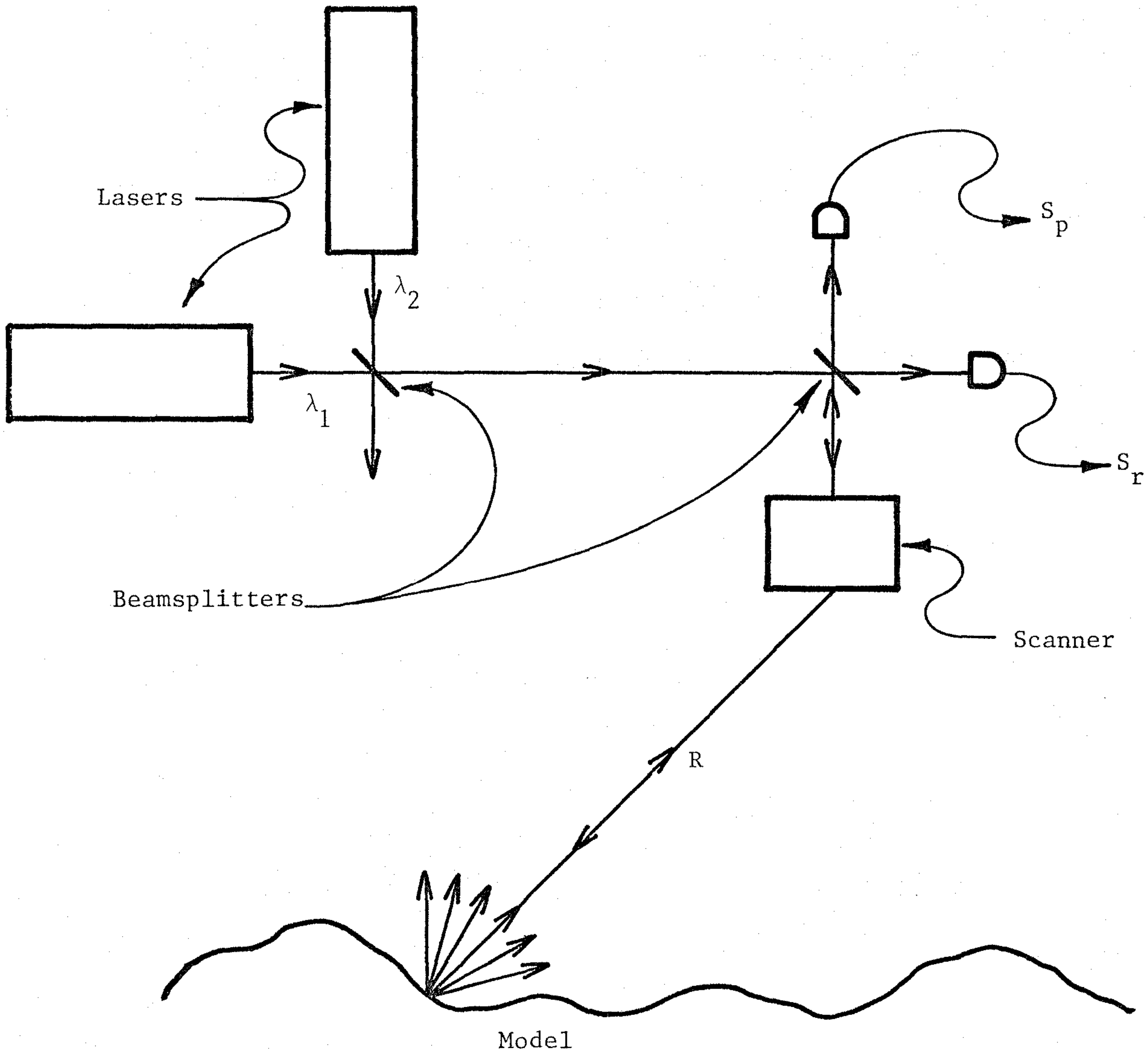

FIGURE 19. A Two-Wavelength Scanning Heterodyne Interferometry System

4.1.1 Beam Alignment

The first thing that must be considered in such a system is the quality of the superimposition of the two laser beams that form the probe, and the effect of a slight angular misalignment. The upper sketch in Figure 20 illustrates the geometry at the detector if the two beams are not perfectly colinear. Assuming they are plane waves, and normalizing their amplitudes for simplicity, the electric fields of the two beams are represented by

$$\begin{aligned} E_1 &= \cos[w_1 t - K_1 (x\sin\gamma_1 + z\cos\gamma_1) - \eta_1] \\ E_2 &= \cos[w_2 t - K_2 (x\sin\gamma_2 + z\cos\gamma_2) - \eta_2] \end{aligned} \qquad (101)$$

where η_1 and η_2 are the distance related phases; w_1 and w_2 are the radian frequencies; K_1 and K_2 are the propagation constants defined by

$$K_n = \frac{w_n}{c} = \frac{2\pi}{\lambda_n} \quad ; \qquad (102)$$

and c is the velocity of light. The detector face is the plane $z = 0$ and, ignoring constants of proportionality, the intensity of the radiation striking it is

$$I = [E_1 + E_2]^2 \Big|_{z = 0} \quad . \qquad (103)$$

Using Equations 101 - 103 and simple trigonometric relationships, the intensity is

$$\begin{aligned} I = 1 &+ \cos[(w_2 - w_1)t - (K_2\sin\gamma_2 - K_1\sin\gamma_1)x - (\eta_2 - \eta_1)] \\ &+ \cos[(w_2 + w_1)t - (K_2\sin\gamma_2 + K_1\sin\gamma_1)x - (\eta_2 + \eta_1)] \\ &+ 1/2 \cos(2w_1 t - 2K_1\sin\gamma_1 x - 2\eta_1) \\ &+ 1/2 \cos(2w_2 t - 2K_2\sin\gamma_2 x - 2\eta_2) \; . \end{aligned} \qquad (104)$$

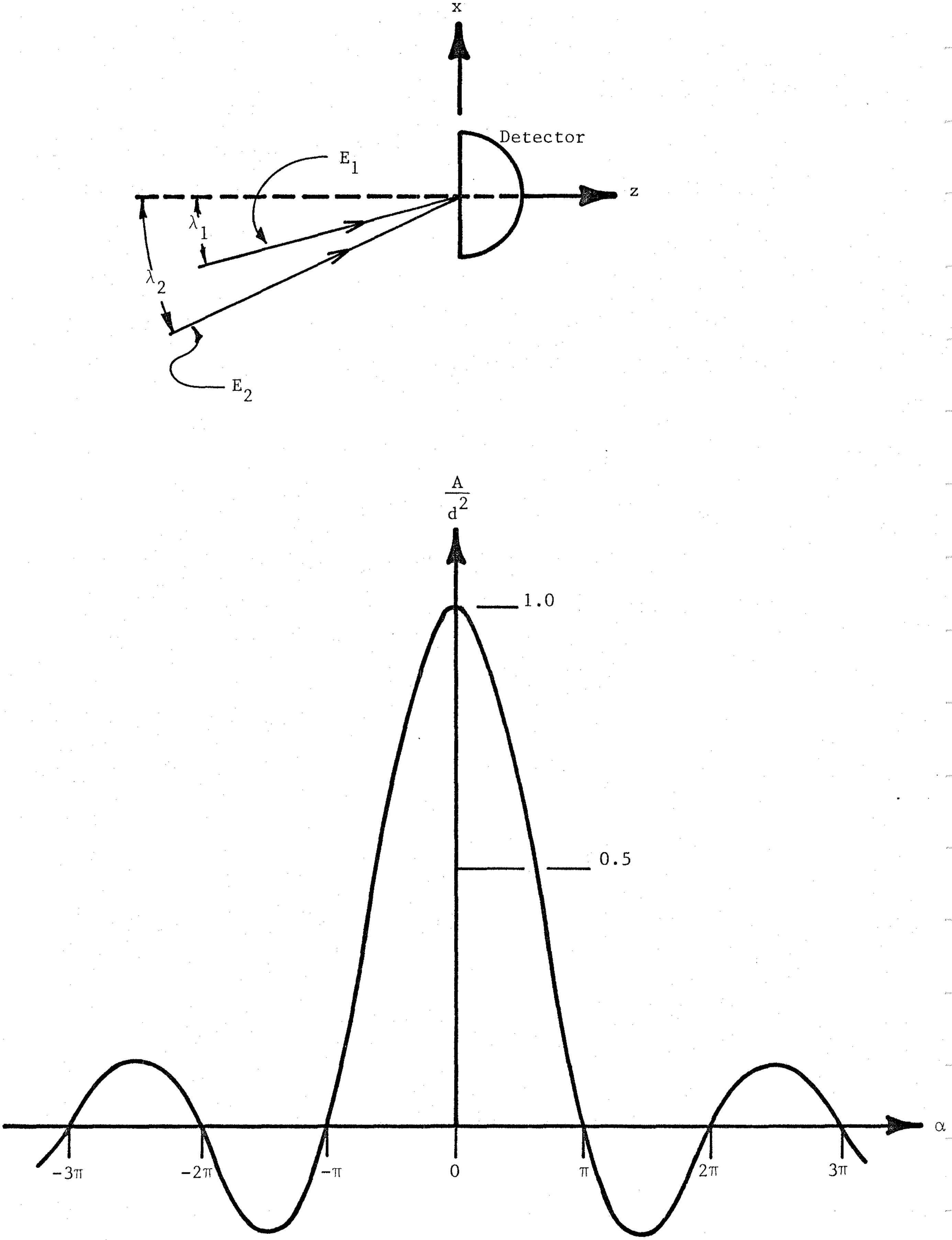

FIGURE 20. Signal Amplitude as a Function of Beam Misalignment

Now optical detectors are square law devices which detect the power that strikes them. However, none are fast enough to detect optical frequencies. Hence, the last three terms in Equation (104) may be dropped without error. Assuming a square detector of dimension dxd, the power on the detector face is

$$P = \iint_{-d/2}^{+d/2} I \, dxdy \quad . \tag{105}$$

Inserting Equation 104 and integrating, this becomes

$$P = d^2 \left\{ 1 + \left[\frac{\sin\alpha}{\alpha} \right] \cos[(w_2 - w_1)t - (\eta_2 - \eta_1)] \right\} \tag{106}$$

where $\alpha = (K_2 \sin\gamma_2 - K_1 \sin\gamma_1) \frac{d}{2}$. (107)

The amplitude of the detected signal is therefore

$$A = d^2 \left[\frac{\sin\alpha}{\alpha} \right] \tag{108}$$

which is plotted as a function of α in Figure 20. Note that the signal is completely lost at integral multiples of π, and considerably reduced at any value above π. Therefore,

$$\alpha \leq \frac{\pi}{2} \tag{109}$$

is chosen as a maximum practical limit for α.

Assuming γ_1 and γ_2 are small enough to make the approximation that

$$\sin\gamma \cong \gamma \ , \tag{110}$$

then, after making the substitution

$$\gamma_2 = \gamma_1 + \Delta\gamma \tag{111}$$

and using Equation 102, Equations 107 and 108 reduce to

$$\Delta\gamma \leq \frac{\lambda_2}{2d} - \frac{v_2 - v_1}{v_2} \gamma_1 \tag{112}$$

where v_1 and v_2 are the cyclic frequencies. Furthermore, assuming that

$$v_2 - v_1 \leq 10 \text{ GHz} \tag{113}$$

the second term on the right side in Equation 112 is negligible, and Equation 112 reduces to

$$\Delta\gamma \leq \frac{\lambda_2}{2d} \quad . \tag{114}$$

Inserting some practical values:

$$\left.\begin{aligned} \gamma_2 &= 0.5 \ \mu\text{m} \\ d &= 0.5 \ \text{mm} \quad ; \end{aligned}\right\} \tag{115}$$

an estimate is obtained of the maximum allowed misalignment:

$$\Delta\gamma \leq .5 \text{ m rad} = 0.029° \quad . \tag{116}$$

Milliradian alignment accuracies of this magnitude over macroscopic distances are probably possible within the vibratory environment of a transonic tunnel. To some degree, however, the vibration will appear as a low frequency modulation of the probe signal, contributing to the overall noise situation. For that reason it will be more advantageous to obtain the two optical frequencies via amplitude modulation of a single laser beam. Since the beam is never split, perfect alignment is inherent and a potential source of noise has been eliminated. Additionally, a single laser and modulator will be more compact than two lasers or a laser and dye laser combination.

4.1.2 Signal Detection and Deflection Measurement

Figure 21 is a revised SHI configuration that employs the modulation scheme outlined in the previous section. The two separate lasers in Figure 19 have been replaced with a single laser and modulator. Furthermore,

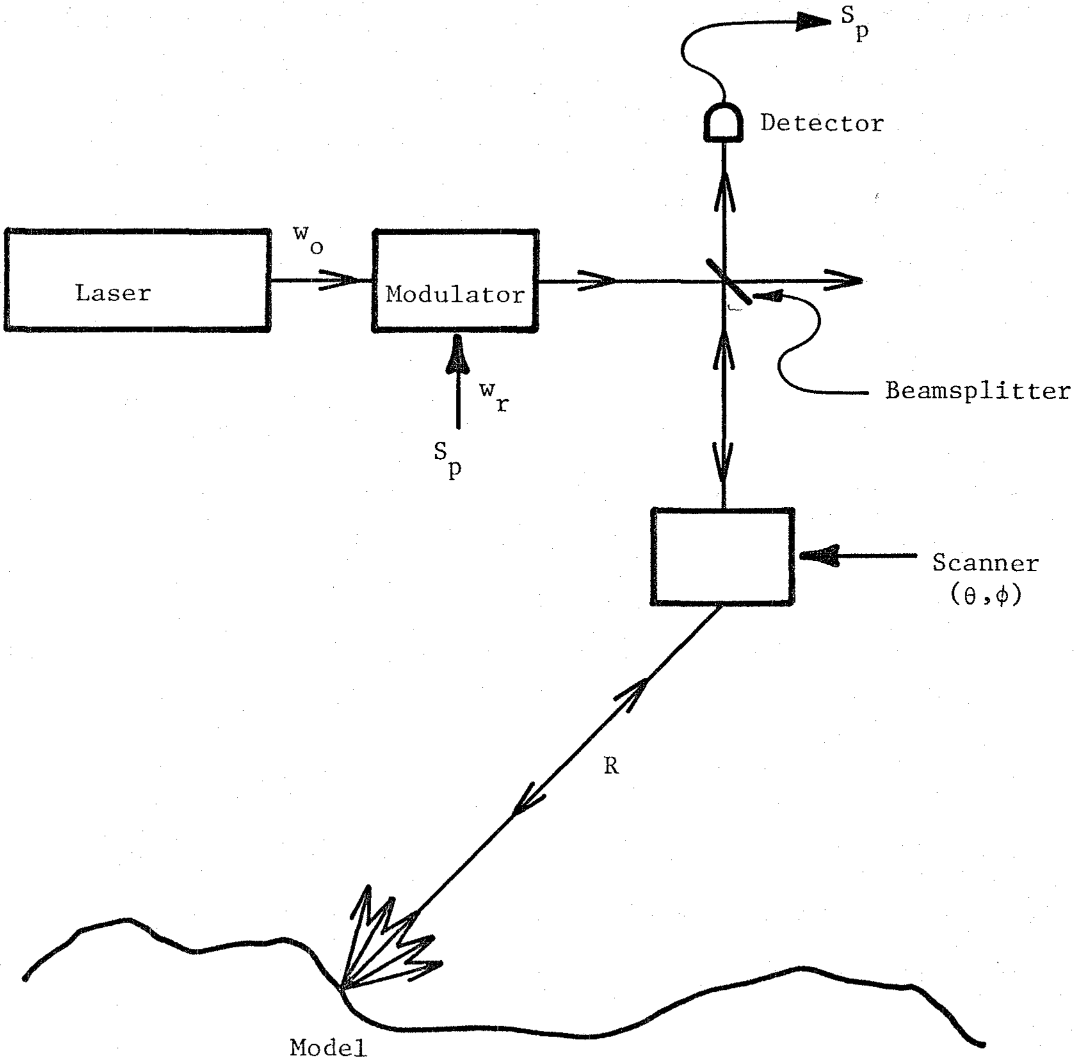

FIGURE 21. Scanning Heterodyne Interferometry with a Modulated Source

the reference signal is generated internally and fed to the modulator as the modulation signal, so there is no need to detect it separately.

The output of the laser is described by the electric field

$$E_o(t) = \cos w_o t \tag{117}$$

and the reference signal by

$$S_r(t) = \cos w_r t \quad . \tag{118}$$

The reference signal modulates the laser radiation so that the output of the modulator is

$$E_m(t) = (a_o + a_r \cos w_r t)\cos w_o t \tag{119}$$

which is merely a double sideband amplitude modulated signal with carrier. At the detector the electric field is

$$E_d(t) = E_m(t - \frac{L+2R}{c}) \tag{120}$$

where R is the variable radial distance from the scanner to the point on the object, L is the sum of the constant internal propagation distances within the system, including any temporal delays within the circuitry, and c is the velocity of light. Since

$$w_r << w_o \tag{121}$$

it is assumed that material dispersion will have a negligible effect on c and λ over the range of optical frequencies considered. Again, ignoring constants of proportionality, the intensity at the detector is

$$I_d(t) = |E_d(t)|^2 \quad . \tag{122}$$

Substituting from Equations 119 and 120, this becomes

$$\begin{aligned} I_d(t) = 1/2 &\left\{a_o + a_r \cos\left[w_r t - \frac{w_r}{c}(L + 2R)\right]\right\}^2 \\ &\bullet \left\{1 + \cos\left[2w_o t - 2\frac{w_o}{c}(L + 2R)\right]\right\} \quad . \end{aligned} \tag{123}$$

And again, since no detector's bandwidth is sufficient to detect optical frequencies, the second term in the second set of brackets is dropped, and the detected probe signal is

$$S_p(t) = \left\{a_o + a_r \cos\left[w_r t - \frac{w_r}{c}(L + 2R)\right]\right\}^2 \tag{124}$$

where constants of proportionality have been ignored. The received signal in Equation 124 consists of the desired fundamental with a second harmonic component that can be removed by filtering if w_r is large compared to the signal bandwidth.

The phase difference between the modulating signal in Equation 118, and the detected probe signal of Equation 124, is therefore

$$\psi = \frac{w_r}{c}(L + 2R) \quad , \tag{125}$$

and the distance to the sample point on the model surface (R) can be determined through Equation 125 by measuring ψ. Furthermore, if R is the required deflection measurement accuracy, then

$$\Delta\psi = 2\frac{w_r}{c}\Delta R \tag{126}$$

is the accuracy required in the measurement of ψ to achieve ΔR. Note that there is a modulo 2π ambiguity in any phase measurement of this kind, and it can be associated with an ambiguity length (λ_a) by adding the 2π equivalent to both sides of Equation 125, i.e.,

$$\psi + 2\pi = \frac{w_r}{c}[L + 2(R + \lambda_a)]. \tag{127}$$

Manipulation of Equations 125 and 127 yields

$$\begin{aligned} \lambda_a &= \frac{c}{2v_r} \\ &= 2\pi\,\frac{\Delta R}{\Delta\psi} \end{aligned} \tag{128}$$

where $$v_r = \frac{w_r}{2\pi} \qquad (129)$$

is the cyclic modulation frequency. Using Equations 126 and 128, Table 3 illustrates the relations between v_r, $\Delta\psi$, and λ_a for the required measurement accuracy listed in Table 1.

TABLE 3

v_r	$\Delta\psi$	λ_a
6.6 MHz	.001°	23.0 m
66.0 MHz	.01°	2.3 m
660.0 MHz	.1°	23.0 cm
6.6 GHz	1.0°	2.3 cm

Obviously, a long ambiguity length is desirable. But that in turn necessitates phase measurement accuracies that may not be practical within the constraints of the NTF.

The accuracy of such a measurement is further limited by point to point variations in the model surface reflectivity, which appear as additional amplitude modulation, albeit at relatively low frequency, of the returning probe signal. This source of noise cannot be eliminated by filtering since its spectral components appear within those of the desired signal, nor by proper surface preparation since even a perfect Lambertian scatterer exhibits a cosine fall off with surface tilt. However, since SHI is a phase sensitive technique, AM noise effects can be minimized by amplitude limiting in a fashion similar to that used in commercial FM systems. But because of the extreme accuracies required within the NTF, the residual effects of such a scheme will appear as phase jitter, and may be of sufficient degree to make other techniques more attractive.

4.1.3 Step Response and Bandwidth

Assume that the probe is raster scanned across the surface of the model, and consider the worst topographic situation that might be encountered: a sharp step in the shape of the model. Now the surface characteristic of the model is derived from the spherical coordinate R, θ, ϕ, which are all parametrically related through time via the raster scan. So the step in the model surface appears as a step in the temporal characteristic of R, which is repeated each raster cycle. It can be said, then, that all model surface characteristics appear as harmonic components of the raster fundamental.

Consider the step function in Figure 22 as a model of this worst case behavior, where Δr is the depth of the step; r_o is the distance to the model; and T_s is the full raster period.

The fundamental component of the received signal will be

$$S_p(t) = \left.\begin{matrix} \cos\left\{w_r t - \frac{w_r}{c}[L + 2(r_o + \Delta r)]\right\} \; ; \; -\frac{t_s}{2} < t < \frac{t_s}{2} \\ \cos\left\{w_r t - \frac{w_r}{c}[L + 2r_o]\right\} \; ; \; \frac{t_s}{2} < t < T_s - \frac{t_s}{2} \end{matrix}\right\} \qquad (130)$$

where $S_p(t)$ was taken from Equation 124 and R was taken from Figure 22.

A Fourier harmonic analysis[10] of Equation 130 yields

$$S_p(t) = \sin\left(\frac{w_r}{c}\Delta r\right) \sin\left\{w_r t - \frac{w_r}{c}\left[L + 2\left(r_o + \frac{\Delta r}{2}\right)\right]\right\} \qquad (131)$$

$$\bullet \sum_{n=1}^{\infty} 4 \, \frac{t_s}{T_s} \, \frac{\sin\left(n\pi \frac{t_s}{T_s}\right)}{\left(n\pi \frac{t_s}{T_s}\right)} \cos(n w_s t) \quad .$$

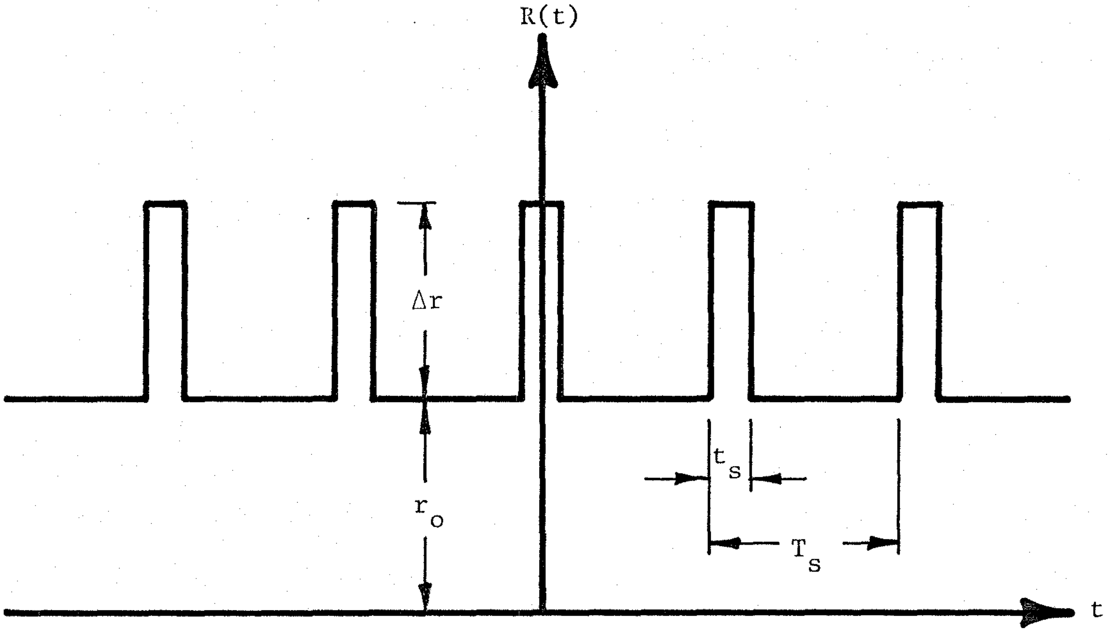

FIGURE 22. Model Surface Step Input

The term within the summation is a result of the phase modulation R(t), and appears as harmonics of w_s located in sidebands about the reference frequency w_r.

If it is desired to sample the entire model surface with a bandwidth of 100 Hz, then a raster frequency of

$$v_s = 300 \text{ Hz} \tag{132}$$

is chosen so as to sample the surface at a rate conservatively beyond that required by the Nyquist sampling criteria[11]. And when considered in conjunction with the reference frequencies of Table 3, the bandwidth required to pass 100 harmonics (60 KHz) is essentially narrow band FM.

Obviously there will be some high frequency components present due to rapid variations in the model surface. But it is unlikely that such surface characteristics will have large amplitudes, and their effect on the probe (phase modulation) will result in minimal frequency deviation[11].

4.2 Optical Homodyne and Heterodyne Detection

It is often possible to improve the signal to noise characteristics of a system of this kind by mixing a portion of the local oscillator (the laser) with the returning signal prior to detection. Consider heterodyne detection, and assume that a portion of the unmodulated laser beam (w_o in Figure 21) is frequency shifted to $w_o+\Delta w$, then mixed with the returning beam prior to detection. Equation 120 then becomes

$$E_d(t) = E_m\left(t - \frac{L + 2R}{c}\right) + a_\ell \cos[w_o + \Delta w)t - \eta_\ell] \tag{133}$$

where $E_m(t)$ is still taken from Equation 119, and η_ℓ is a constant phase term included for generality. As before, squaring Equation 133 to obtain the intensity, and dropping DC components and terms with frequency components beyond the bandwidth of the detector, the detected probe signal in Equation 124 becomes

$$S_p(t) = a_o a_r \cos(w_r t - \phi_r) - \frac{a_r^2}{4} \cos[2(w_r t - \phi_r)] + a_\ell [a_o + a_r \cos(w_r t - \phi_r)] \cos(\Delta w t - \eta_\ell + \phi_o) \tag{134}$$

where $\phi_r = \frac{w_r}{c} (L + 2R)$ (135)

$$\phi_o = \frac{w_o}{c} (L + 2R) \quad . \tag{136}$$

Figure 23 is a plot of the power spectral density of the signal of Equation 134. Note that the first two terms appear as phase modulation sidebands about center frequencies w_r and $2w_r$, which are the fundamental and second harmonic distortion signals of the original detection scheme. These are identical to the signals received in Equation 124. The third term in Equation 134 represents the received heterodyne signal which, if $a_\ell > a_r$, is a stronger signal than the fundamental, and appears as a carrier at w' with sidebands that are replicas of the fundamental signal.

The difficulty here is that w' is not merely Δw, as might be assumed at first glance. Rather, it is the instantaneous frequency of the last cosine term appearing in Equation 134, which is

$$w' = \frac{d}{dt} (\Delta w t - \eta_\ell + \phi_o) = \Delta w + \frac{d\phi_o}{dt} \tag{137}$$

Substituting Equation 136 into Equation 137 yields

$$w' = \Delta w + 2 \frac{w_o}{c} \frac{dR}{dt} \quad . \tag{138}$$

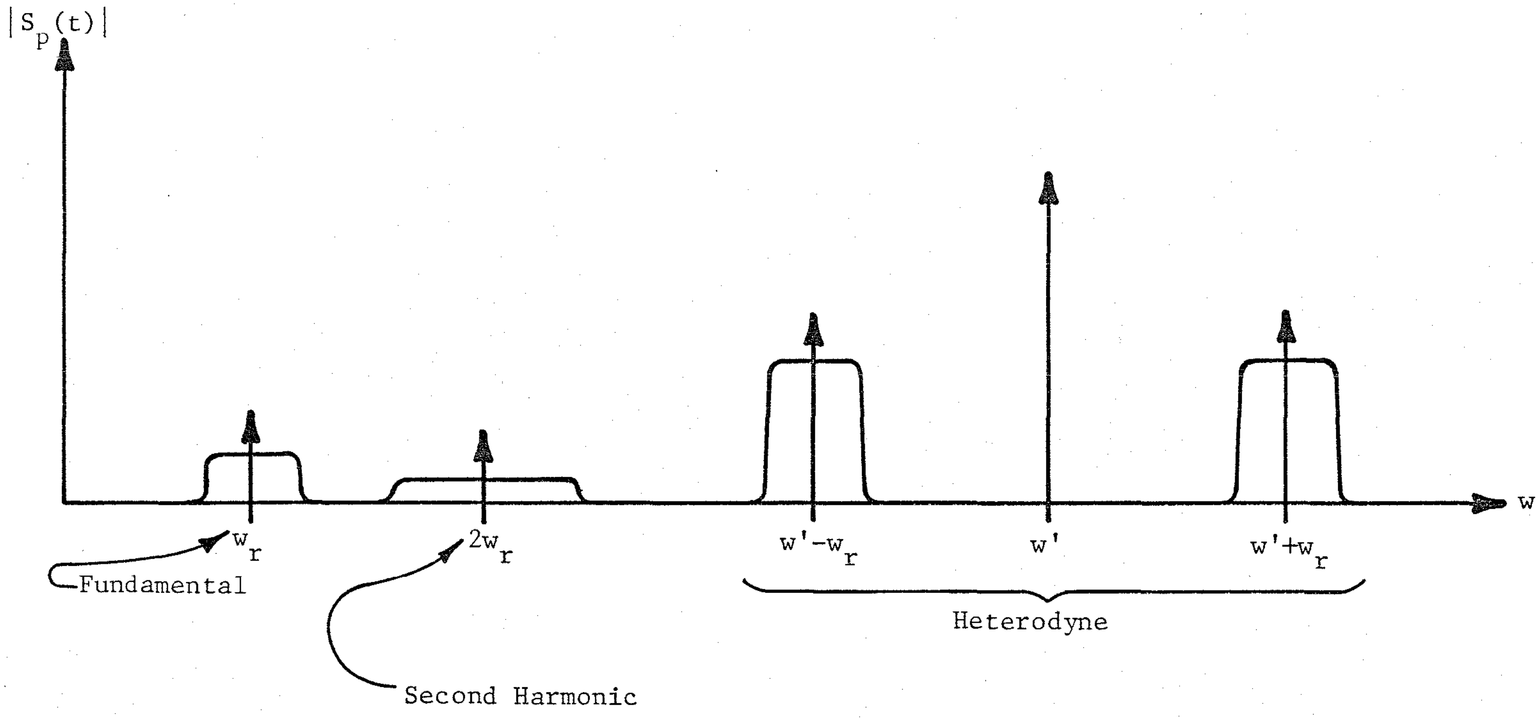

FIGURE 23. The Power Spectral Density of the Received Optical Heterodyne Signal

And from Equation 102,

$$w' = w + \frac{4\pi}{\lambda_o}\frac{dR}{dt} \tag{139}$$

where λ_o is the laser wavelength ($\cong .6\mu m$). Now R's temporal variation may be relatively slow, but λ_o is so small compared to potential values of dR, that the second term in Equation 137 is likely to dominate, producing a rapidly and randomly varying carrier frequency (w').

A physical interpretation of this phenomenon is that the original sensitivity of standard interferometry ($\lambda_o/2$), which was too great to begin with, has been regained to the detriment of the system. For that reason, optical heterodyne and homodyne detection are not feasible in a system of this nature.

4.3 Phase Locked Loop Detection

Table 3 illustrates the most fundamental difficulty that will be encountered in an SHI system, and that is: even at high modulation frequencies, extremely accurate phase measurements are required to obtain the desired deflection measurement accuracy. A typical vector voltmeter of high quality* can measure phase differences with an accuracy of ±1.50 at frequencies between 1 MHz and 1 GHz. But this instrument is a narrow band device (1 KHz) and not capable of tracking a rapidly varying signal. It is unlikely, therefore, that such a straight forward approach will have both sufficient speed and accuracy to be applicable in this program. However, the advent of phase locked loop (PLL)[12,13] technology in recent years offers an alternate approach with some potential.

---

* Hewlett Packard Model 8405A

The PLL technique in this application converts the phase measurement to a frequency measurement by nulling the phase error. This is done by altering the modulation frequency (w_r) so that the round trip path length (L + 2R) corresponds to one cycle of the modulation frequency, i.e.

$$\frac{w_r}{c}(L + 2R) = 2\pi \quad . \tag{140}$$

The resulting phase difference between the probe and reference signals has been removed, and R is obtained by measuring w_r and inverting Equation 140 to yield

$$R = \frac{c}{2v_r} - \frac{L}{2} \quad . \tag{141}$$

A differential measurement ΔR can be obtained from

$$\Delta R = -\frac{c}{2v_r}\frac{\Delta v_r}{v_r} \quad . \tag{142}$$

And if the second term on the right side of Equation 141 is negligible, then

$$\frac{\Delta R}{R} \cong \frac{\Delta v_r}{v_r} \quad . \tag{143}$$

Within the NTF,

$$\left.\begin{aligned} R &\cong 1.2 \text{ meter} \\ \Delta R &= 64\ \mu\text{m} \quad . \end{aligned}\right\} \tag{144}$$

And from Equations 141-143

$$\left.\begin{aligned} \frac{R}{\Delta R} &= 18{,}750 \\ v_r &= 125 \text{ MHz} \ . \end{aligned}\right\} \tag{145}$$

v_r would have to be measured accurately to 1 part in 18,750, which is not terribly restrictive, and would allow almost 7,000 samples per second. A raster scan of 300 Hz sampling 100 spots per scan requires 30,000 samples per second, so the above sample rate is not sufficient, although it is at least approaching that required.

4.4 Laboratory Experiments

To gain insight into the PLL approach, the contractor fabricated a laboratory experiment of the configuration illustrated in Figure 24. A Laser Diode Laboratories, Inc., IRE 160 high frequency optical communications light emitting diode was used as the radiative source because it was an affordable and convenient means of modulated optical power. The radiated energy was collected by a microscope objective and formed to an intermediate image at a short distance (16 cm). It was then reimaged by a projection lens onto a scattering target at a distance of 11.1 meters. The scattered radiation was collected onto the cathode of a Hamamatsu R666 photomultiplier tube. The output of the PMT was amplified then fed into a TTL comparator for conversion to TTL levels. The Phase Detector was an edge triggered device which produced a voltage that was proportional to the phase difference between the comparator output and the voltage controlled oscillator. Included within the loop were an integrator for loop stability and a differential amplifier that made it possible for the loop to lock at a phase difference other than 2π. Therefore, for the purposes of this experiment, Equation 140 is modified in the following fashion,

$$\frac{w_r}{c}(L + 2R) = K2\pi \qquad (146)$$

where $0 \leq K \leq 1$. Using the relationship

$$w_r = 2\pi v_r \qquad (147)$$

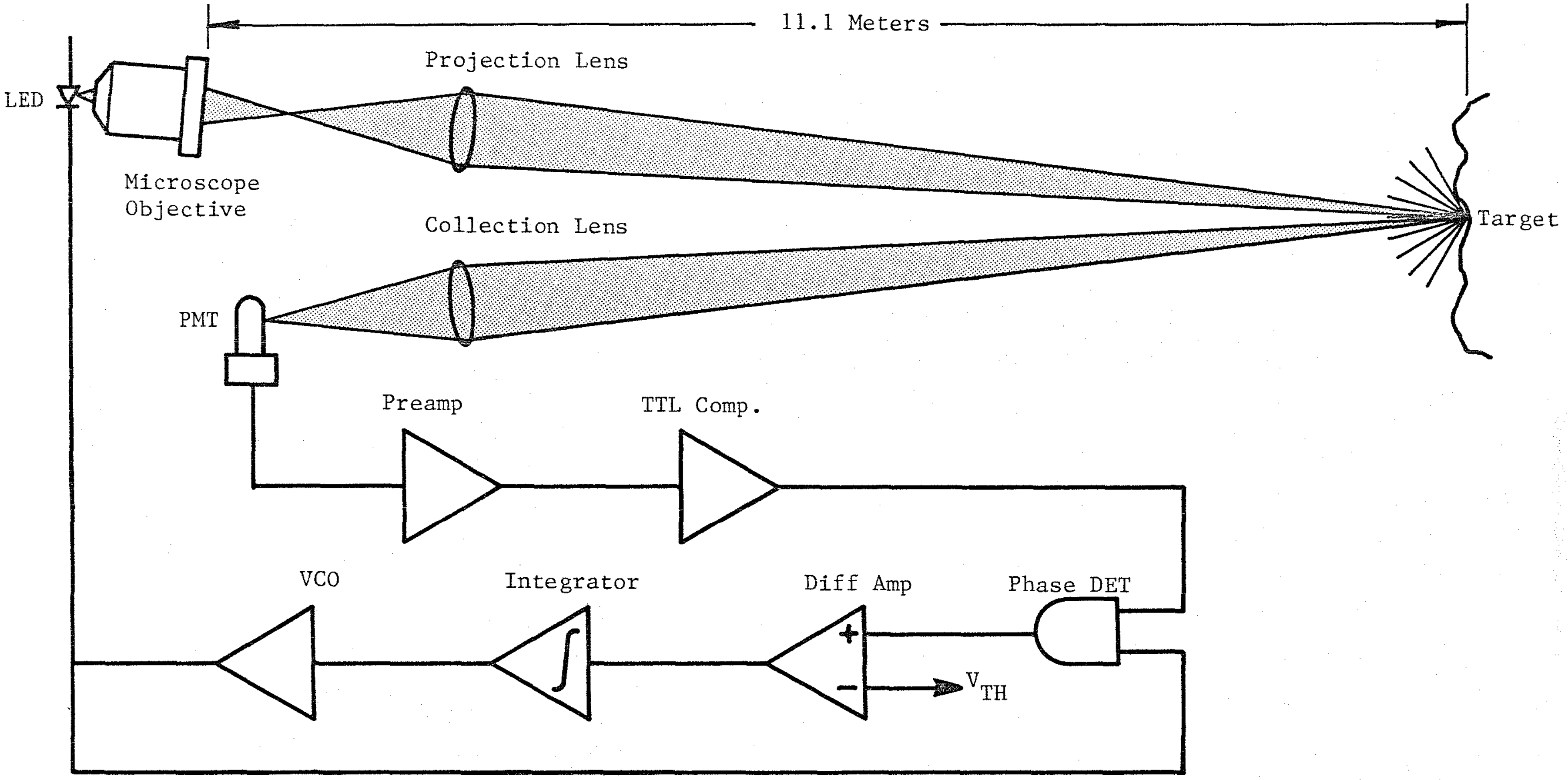

FIGURE 24. The Configuration of the Limited Scale Scanning Heterodyne Interferometry Mock-Up

equation 146 becomes

$$v_r\ (L + 2R) = Kc \quad . \tag{148}$$

Note that L is a constant length that includes circuit delays as well as optical path lengths not included in R. The purpose behind including the constant K in the loop was so that it would operate over reasonable laboratory distances (<15 meters) yet remain within the modulation bandwidth of the LED (10 MHz).

When the loop was operating, it exhibited the following baseline characteristics:

$$\left.\begin{aligned} & v_{ro} = 4.100 \text{ MHz} \\ \text{at} \quad & R_o = 11.1 \text{ meters} \end{aligned}\right\} \tag{149}$$

The short term (~0.1 sec) frequency stability was measured by observing the degree of flicker in the reading on the digital frequency counter. It was

$$\Delta v_s \leq \pm 0.001 \text{ MHz} \quad . \tag{150}$$

The long term (~10 sec) frequency stability (drift) was observed to be better than

$$\Delta v_L \leq \pm 0.02 \text{ MHz} \quad . \tag{151}$$

The frequency (v_r) was measured at several points as R was decreased from the baseline value listed in Equation 149. The results are graphed in Figure 25, where ΔR is the difference between R and R_o. Inserting the relationship

$$R = R_o - \Delta R \tag{152}$$

into Equation 148 yields

$$v_r = \frac{cK}{L + 2(R_o - \Delta R)} \quad . \tag{153}$$

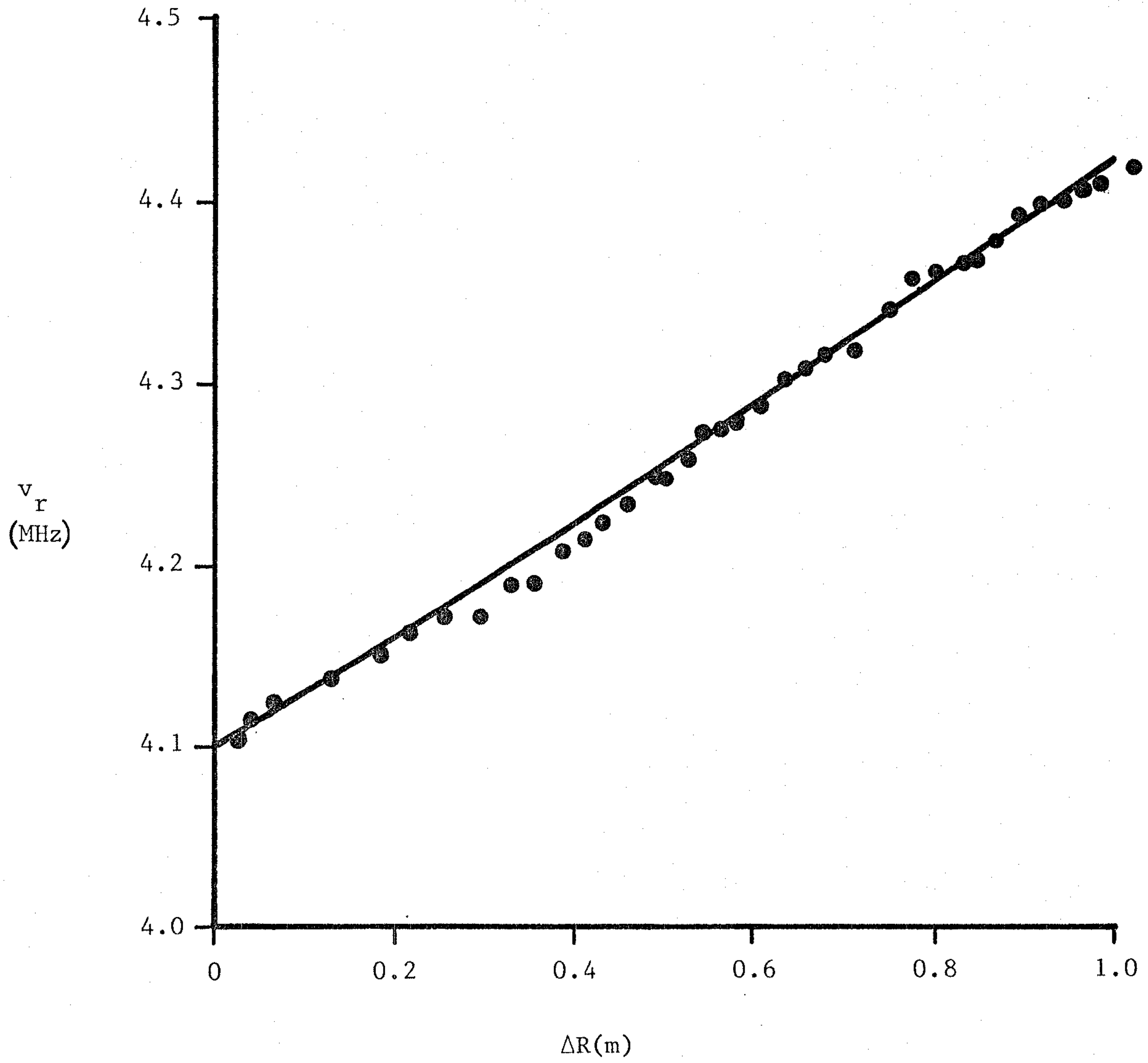

FIGURE 25. The Frequency Variation of the SHI Mock-Up with Changing Target Distance R

The solid line in Figure 25 is a plot of Equation 153 using the constant values

$$\left.\begin{aligned} K &= 0.372 \\ L &= 5.031 \text{ meters} \quad . \end{aligned}\right\} \quad (154)$$

The fit is quite good, verifying the applicability of Equation 148. Any lack of fit appears to be due to long term frequency instability.

Next, differentiating both sides of Equation 148, and manipulating the results yields

$$\Delta R = \left(R + \frac{L}{2}\right) \frac{\Delta v_r}{v_r} \quad . \qquad (155)$$

Inserting values from Equations 149, 150, and 154, the short term measurement accuracy is computed to have been

$$\Delta R = \pm 3.3 \text{ mm} \quad . \qquad (156)$$

This is obviously not sufficient for deflection measurements within the NTF. But this experiment was not intended to provide that degree of sophistication. Higher baseline frequencies and shorter baseline distances should greatly improve both stability and accuracy.

5.0 CONTOUR HOLOGRAPHY

One of the most dramatic phenomena to emerge from the field of holography is the ability to acquire interferometric data from diffusely scattering surfaces. Such a capability is, of necessity, impossible with standard interferometry. But the hologram, which by its very nature stores a fully coherent image of the diffuse object, is capable of recording two images in such a fashion that they reconstruct at the same location in space, and interfere on a point by point basis. This is one form of holographic interferometry[14], and the fringes that result are a function of changes that have occurred in the object surface between the two recordings. Contour holography[15] is another form of holographic interferometry where the two images are recorded simultaneously, or nearly so, but at different wavelengths. Upon reconstruction the two images are microscopically displaced because of the differences in recording wavelength, and fringes result that are a function of the wavelengths and the surface topography.

5.1 Basic Holographic Recording and Reconstruction

Figure 26 illustrates the basic geometry of holographic recording and reconstruction. U_o represents the object wave to be recorded, which may have an extremely complex spatial nature, and U_r represents a reproducibly pure reference wave. The two waves must be coherently related so that they produce a stationary interference pattern at points in space where they are coincident. A hologram is fabricated by recording this interference pattern in the emulsion of a photographic plate, producing a diffraction grating with a complexity that is entirely dependent upon the complexity of the two waves and how they interfere.

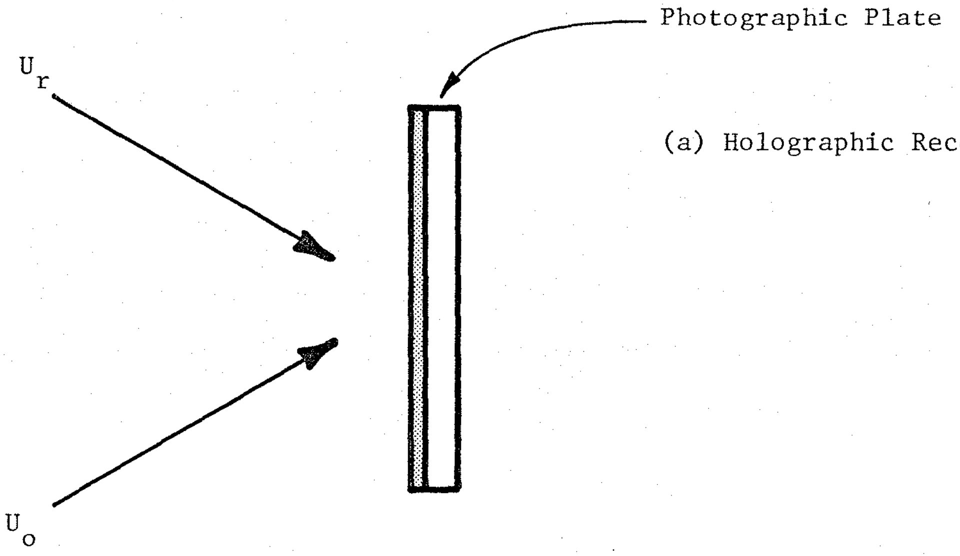

(a) Holographic Recording

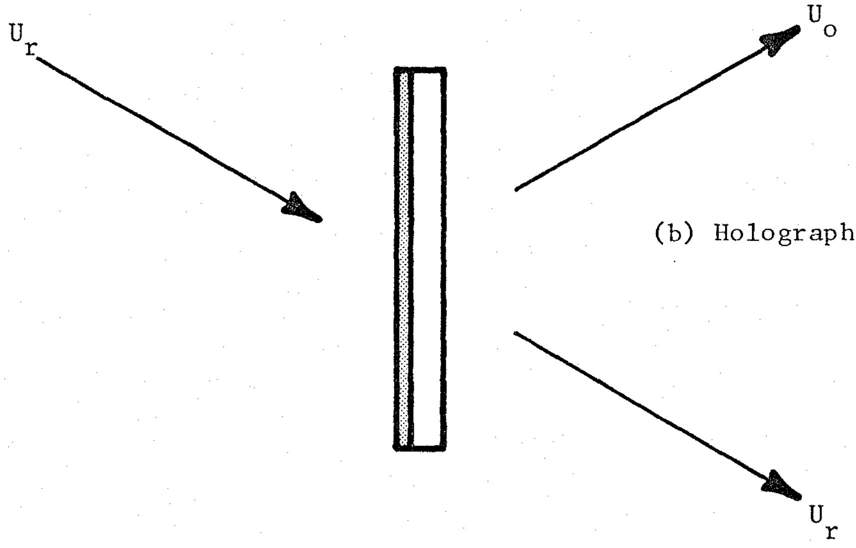

(b) Holographic Reconstruction

FIGURE 26. Recording and Reconstruction of a Simple Hologram

To reconstruct the hologram, the photographic emulsion is first developed to bring out the diffraction pattern, then reilluminated with the reproducible reference wave U_r. The filtering effect of this complex grating is to diffract a significant amount of the reference wave into a reproduction of the object wave, with its original complexity maintained and reproduced in its entirety, as in Figure 26b. The hologram appears to be a window through which the original object may be viewed in its full three-dimensional character.

As stated earlier, the object and reference waves must be coherently related, hence, the use of a single laser from which both waves are acquired by beamsplitting. Keeping this in mind, Figures 27a and b illustrate two basic geometries for recording a hologram. In both, the output of a single laser is passed through a beamsplitter (BS) for division into object and reference waves, and the reference beam is passed unperturbed to the holographic plate. Also in both, the objects diffusely reflect (scatter) the light that is incident upon them. In the single pass configuration of Figure 27a the object wave, after scattering from the object, impinges directly upon the holographic plate. Whereas in the double pass configuration of Figure 27b, the scattered object wave is recorded through the beamsplitter.

A diffuse object may be considered an infinite number of infinitesimal points, each of which scatters the incident radiation into a hemisphere. At a point in the photographic emulsion of the holographic plate, the resultant electric field is the integral of the contributions from all points on the object surface. The situation may, however, be analyzed by considering a single point on the object surface and its recording and

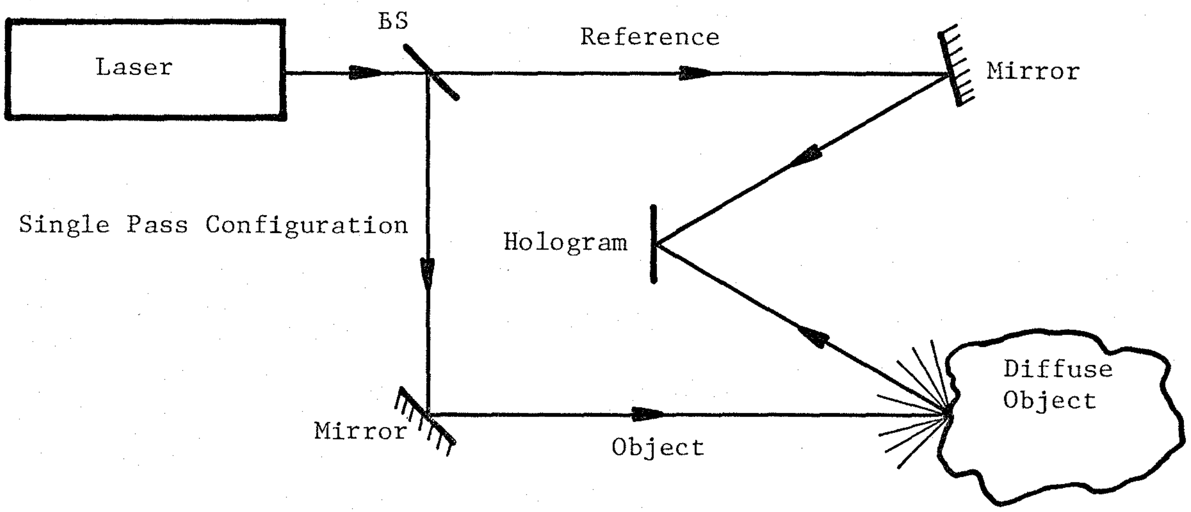

(a) Single Pass Configuration

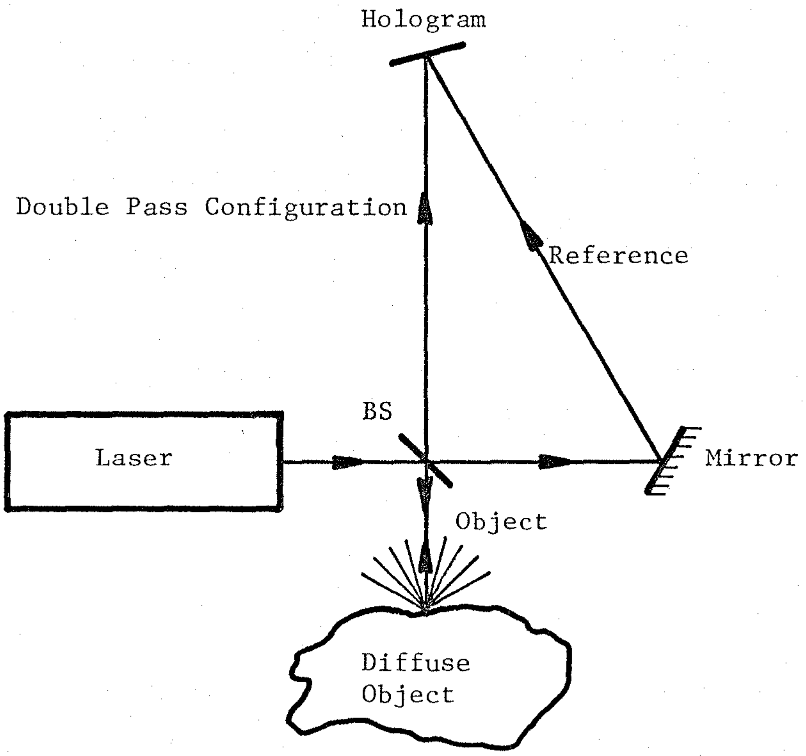

(b) Double Pass Configuration

FIGURE 27. The Basic Geometries for Recording a Hologram of a Diffuse Object.

reconstruction characteristics. Such a simplified analysis is valid if the recording medium is linear, which is most often the case in holography since one effect of the reference wave is to bias the emulsion into the linear region of its operating characteristic.

Goodman[16] provides an excellent point source analysis of the holographic process. With certain changes in notation his results are repeated here. Figure 28 illustrates the geometry of both recording and reconstruction. The emulsion of the holographic plate occupies the (x,y,0) plane. A point source of wavelength λ_1 located at (x_s,y_s,z_s) illuminates the object point (x_o,y_o,z_o) which scatters radiation to the point (x,y,0) in the photographic emulsion. With an insignificant loss of generality, the reference beam is assumed to be collimated with direction cosines $(\alpha_r,\beta_r,\gamma_r)$ and wavelength λ_1. The reference beam and the scattered radiation from the object point mix at the photographic emulsion where their interference pattern is recorded.

After the plate is developed, it is reilluminated with a collimated reference beam, but this time with direction cosines $(\alpha_c,\beta_c,\gamma_c)$ and wavelength λ_c. The reconstructed image point is a virtual image that appears at (x_i,y_i,z_i) where

$$\left.\begin{aligned} \frac{x_{i1}}{R_{io1}} &= \alpha_c + \frac{\lambda_c}{\lambda_1}\left(\frac{x_o}{R_{oo}} - \alpha_{r1}\right) \\ \frac{y_{i1}}{R_{io1}} &= \beta_c + \frac{\lambda_c}{\lambda_1}\left(\frac{y_o}{R_{oo}} - \beta_{r1}\right) \\ \frac{1}{R_{io1}} &= \frac{\lambda_c}{\lambda_1}\ \frac{1}{R_{oo}} \end{aligned}\right\} \qquad (157)$$

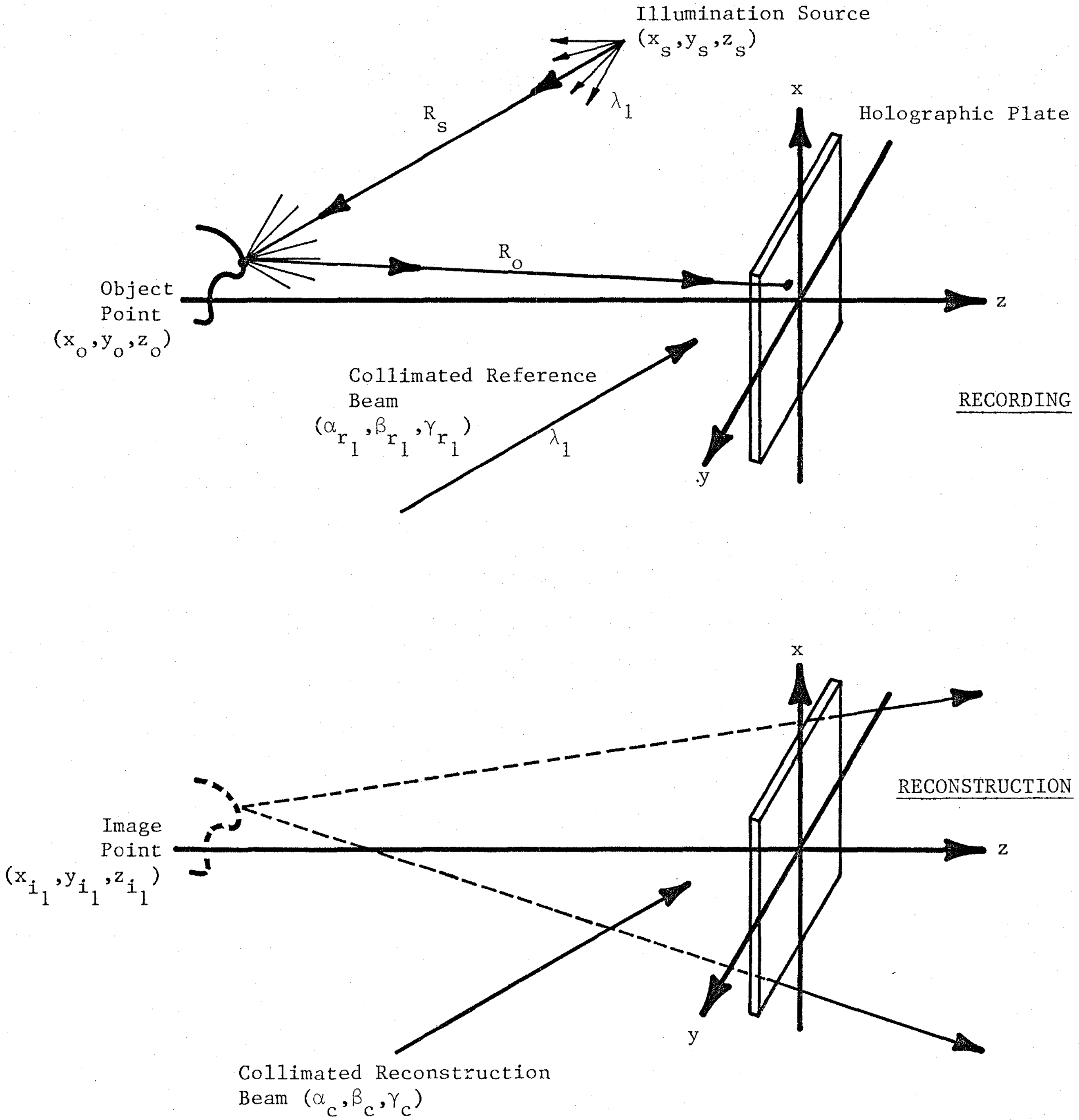

FIGURE 28. Recording and Reconstruction Geometry and Notation

$$\left.\begin{aligned} R_{io1}^{2} &= x_{i1}^{2} + y_{ci}^{2} + z_{i1}^{2} \\ R_{oo}^{2} &= x_{o}^{2} + y_{o}^{2} + z_{o}^{2} \end{aligned}\right\} \text{(157) Con't.}$$

Note that when the reference beam is unchanged from recording to reconstruction, i.e.

$$\left.\begin{aligned} &(\alpha_c,\beta_c,\gamma_c,) = (\alpha_{r1},\beta_{r1},\gamma_{r1}) \\ \text{and}\quad &\lambda_c = \lambda_{r1}, \end{aligned}\right\} \text{(158)}$$

then the image is undistorted and unmagnified, i.e.

$$(x_{i1},y_{i1},z_{i1}) = (x_o,y_o,z_o) \quad . \tag{159}$$

There is also a real image that appears during reconstruction in addition to the virtual image discussed above. Under the right circumstances, however, the two images are spatially separate and do not interact. For that reason, and to maintain clarity and simplicity, the real image is not considered here, though the contouring relationships hold for both images, and the possibility always exists of using the real image to advantage.

5.2 Multiple Wavelength Contour Holography

To induce contour fringes on the surface of the image, the geometries of Figure 28 and the procedures involved remain relatively unchanged. The holographic plate is, however, exposed twice: once with the object illumination and reference beam at wavelength λ_1; and a second time with both changed to wavelength λ_2. In this way, two interference patterns are recorded in the photographic emulsion and two images result upon reconstruction. It should be noted here that the two exposures may be performed simultaneously since, by their very nature, the two wavelengths will not interact to produce a third stationary interference pattern. In the event, however, that the exposures are performed separately, care must be taken to insure that

1) the object is stationary between exposures, or
2) the time that ellapses between exposures is short enough that object motion is insignificant ($<\lambda/2$).

If significant object motion does occur between exposures, extraneous interferometric fringes will appear in addition to the desired contours. And since the interferometric sensitivity ($\lambda/2$) is much less than the contour spacing, the undesired fringes will most likely dominate.

To extend the analysis of the previous section to contour holography, but retain the necessary generality, three different reference beams are used for 1) the first recording (subscript 1), 2) the second recording (subscript 2), and 3) reconstruction (subscript c). Equation 157 remains valid for determining the location of the first image point (x_{i1},y_{i1},z_{i1}), and can be modified to determine the second image point (x_{i2},y_{i2},z_{i2}) by merely replacing the subscript 1 with the subscript 2. Now, if the three reference beams are adjusted so that

$$\left.\begin{aligned} \frac{\alpha_{r1}}{\lambda_1} &= \frac{\alpha_{r2}}{\lambda_2} = \frac{\alpha_c}{\lambda_c} \\ \frac{\beta_{r1}}{\lambda_1} &= \frac{\beta_{r2}}{\lambda_2} = \frac{\beta_c}{\lambda_c} \end{aligned}\right\} \quad (160)$$

then the image relationships reduce to

$$\left.\begin{aligned} x_{i1} &= x_{i2} = x_o \\ y_{i1} &= y_{i2} = y_o \end{aligned}\right\} \quad (161)$$

$$\left.\begin{aligned}&\frac{\lambda_1}{R_{i01}} = \frac{\lambda_2}{R_{i02}} = \frac{\lambda_c}{R_{oo}}\\&z_{i1}{}^2 = R_{io1}{}^2 - x_o{}^2 - y_o{}^2\\&z_{i2}{}^2 = R_{io2}{}^2 - x_o{}^2 - y_o{}^2\end{aligned}\right\} \begin{array}{l}(161)\\ \text{con't.}\end{array}$$

and the location of the fringes is described by[15]

$$R_s + R_o = \left|\frac{\lambda_1\lambda_2}{\lambda_1-\lambda_2}\right| N \tag{162}$$

$$\left.\begin{aligned}\text{where}\quad &R_o{}^2 = (x_o-x)^2 + (y_o-y)^2 + z_o{}^2\\&R_s{}^2 = (x_o-x_s)^2 + (y_o-y_s)^2 + (z_o-z_s)^2 \quad .\end{aligned}\right\} (163)$$

The contour fringes in the object space (x_o,y_o,z_o) described by Equations 162 and 163 are merely a series of concentric ellipsoids of revolution with foci located at the point of the illumination source (x_s,y_s,z_s) and the viewing point $(x,y,0)$, as illustrated in Figure 29. The major axis (2a) and minor axis (2b) are determined by

$$\left.\begin{aligned}&a = \frac{1}{2}\left|\frac{\lambda_1\lambda_2}{\lambda_1-\lambda_2}\right| N\\&b^2 = a^2 - (x_s-x)^2 - (y_s-y)^2 - z_s{}^2 \quad .\end{aligned}\right\} (164)$$

The contours are spaced by

$$\left.\begin{aligned}&\Delta a = \frac{1}{2}\left|\frac{\lambda_1\lambda_2}{\lambda_1-\lambda_2}\right|\\&\Delta b = \frac{a}{b}\,\Delta a \quad .\end{aligned}\right\} (165)$$

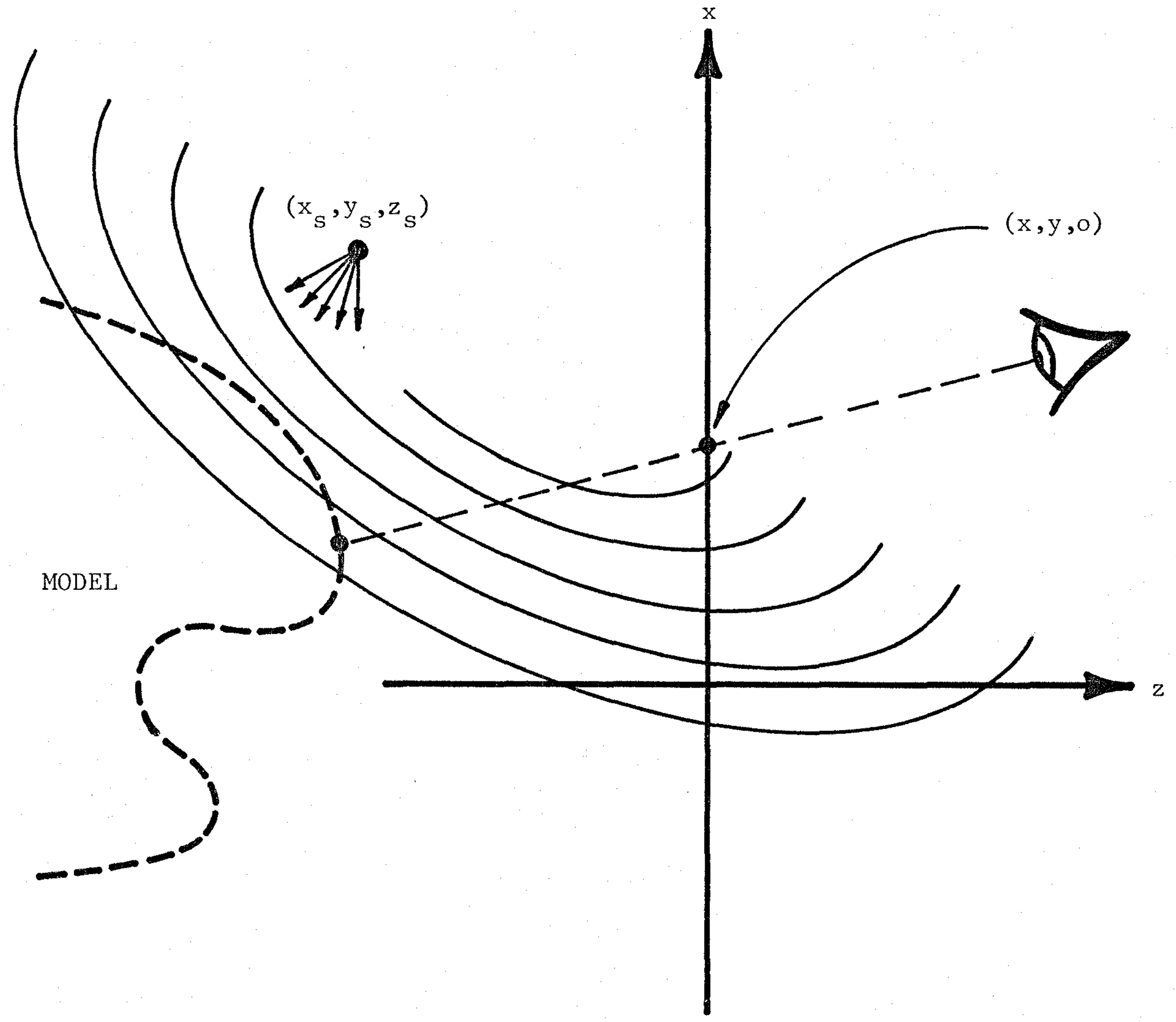

FIGURE 29. The Contour Fringes Generated by 2 Wavelength Holographic Contouring.

Note that as the viewing aperture (the pupil of the eye in Figure 29) observes different object points, its line of sight passes through different points on the holographic plate. Hence, the position of one of the elliptical foci is a function of the object point viewed, and the overall elliptical contour pattern is distorted. This can be alleviated by locating the viewing aperture in the plane of the hologram so that the point through which the line of sight passes is constant for all object points.

There are also certain limitations that must be adhered to if the contour fringes are to be at all visible, let alone with any reasonable contrast. Consider the situation depicted in Figure 30, where the viewing aperture is located in the plane of the hologram at the origin of the coordinate system. The two image points observed by the viewing system interfere and produce fringes only if they are both located within the resolution volume (Airy disc x depth of focus: see Section 3.2.1) of the viewing system[15]. Now along the line of sight to a particular object point, the two image points are observed as having a transverse displacement (ε_T) and a longitudinal displacement (ε_L). Therefore, from Equations 31 and 33

$$\left.\begin{aligned} \varepsilon_T &\leq D_s = 2.44\lambda\left(\frac{L}{D}\right) \\ \varepsilon_L &\leq 2\varepsilon = 4.88\lambda\left(\frac{L}{D}\right)^2 \quad . \end{aligned}\right\} \quad (166)$$

Recognizing that commonly

$$\frac{L}{D} > 1 \quad , \quad (167)$$

the first of the requirements in Equation 166 is obviously the most restrictive. It is for that reason that a telecentric viewing lens (see Section 3.2.1), if at all feasible, should be used to observe the

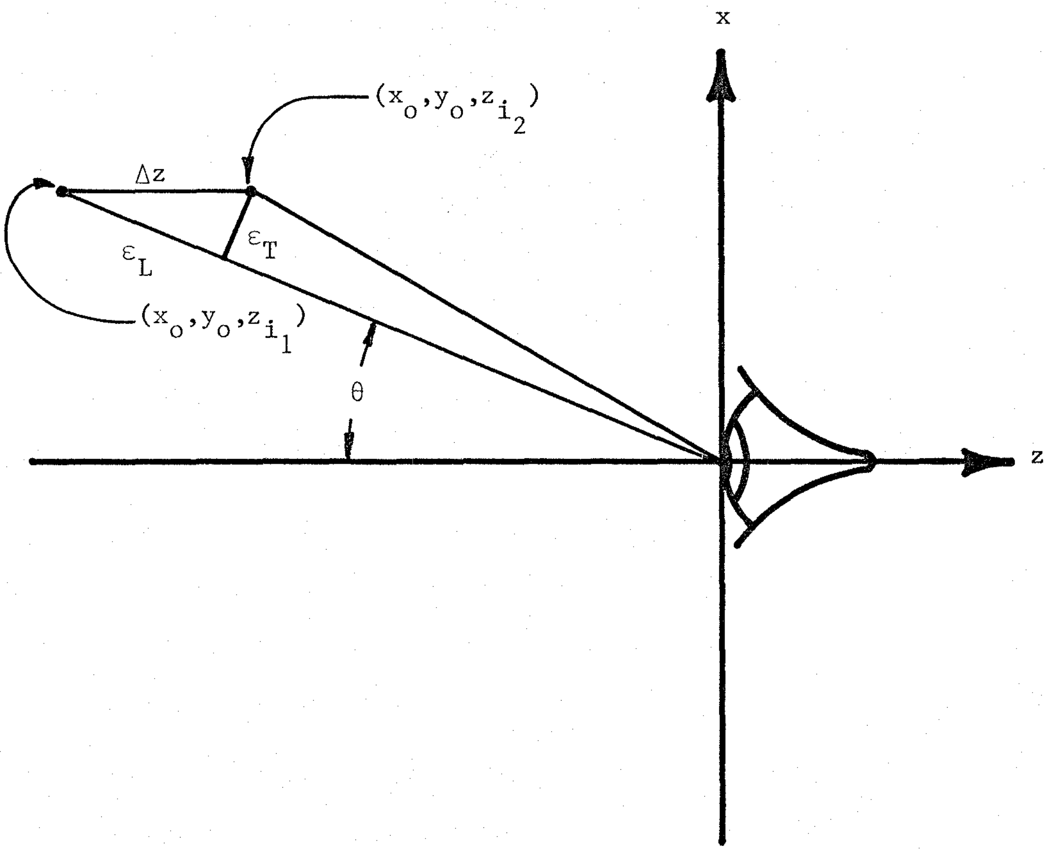

FIGURE 30. The Relative Positions of the Observed Image Points

contour fringes during reconstruction. By locating the aperture stop in the back focal plane of the lens, the entrance pupil, rather than the exit pupil as in the earlier case, is located at infinity and the line of sight for all object points is parallel to the optic axis; ε_T is identically reduced to zero, removing the first restriction of Equation 166; and ε_L is equal to the image point displacement (Δz) where

$$\Delta z = |z_{i1} - z_{i2}| \quad . \tag{168}$$

Therefore, from the second of Equation 166,

$$\Delta z \leq 4.88\lambda_c \left(\frac{L}{D_L}\right)^2 \tag{169}$$

and from Equation 161, if $\Delta z << z_o$, then

$$\Delta z \cong \frac{R_{oo}^2}{\lambda_c z_o} \Delta\lambda \quad . \tag{170}$$

The telecentric configuration described above yields fringes that are paraboloids of revolution with a focus at (x_s, y_s, z_s) and a directrix that is the plane described by

$$z = -\left|\frac{\lambda_1 \lambda_2}{\lambda_1 - \lambda_2}\right| N \quad . \tag{171}$$

5.3 Contour Holography Within the NTF

Ideally, the contours generated on the image of the model surface should be planar. But to accomplish that the illumination source point must be located at infinity (a collimated beam), requiring, like moiré, collimating optics and tunnel windows the size of the model (1 meter). Obviously, such a system is impractical, so more complex geometrical contours must be accommodated. But where moiré was hampered by the necessarily large depth of focus, which indirectly limited the contour spacing, the contours of a multiple wavelength holographic system are independent of the imaging optics, as evidenced by Equations 165. Furthermore holographic contouring does not yield the extraneous fringes that can be so detrimental in a moiré system.

Consider the system depicted in Figure 31. It is only one of many possible configurations but it illustrates the technique. A telecentric imaging lens, with its aperture located in the front focal plane, which is immediately behind a tunnel window, forms an image of the model near the holographic plate during recording. Varner[17] has shown that a properly corrected lens in the recording process does not influence the contour locations as they relate to object space.

Note the beamsplitter located between the imaging lens and the holographic plate. It serves two functions, both of which are illustrated in a separate partial figure so as not to clutter the complete system representation. Its first function is to allow the reference beam to be brought in from off axis so that it strikes the holographic plate at the proper angle for optimum recording (≈30°). Its second function is to allow a collimated illumination beam to be brought in from the other side and reflected into the tunnel. The imaging lens also serves a second purpose by focusing the illumination beam to a point in the aperture of the imaging lens. And keep in mind that these functions occur simultaneously with imaging during the recording process.

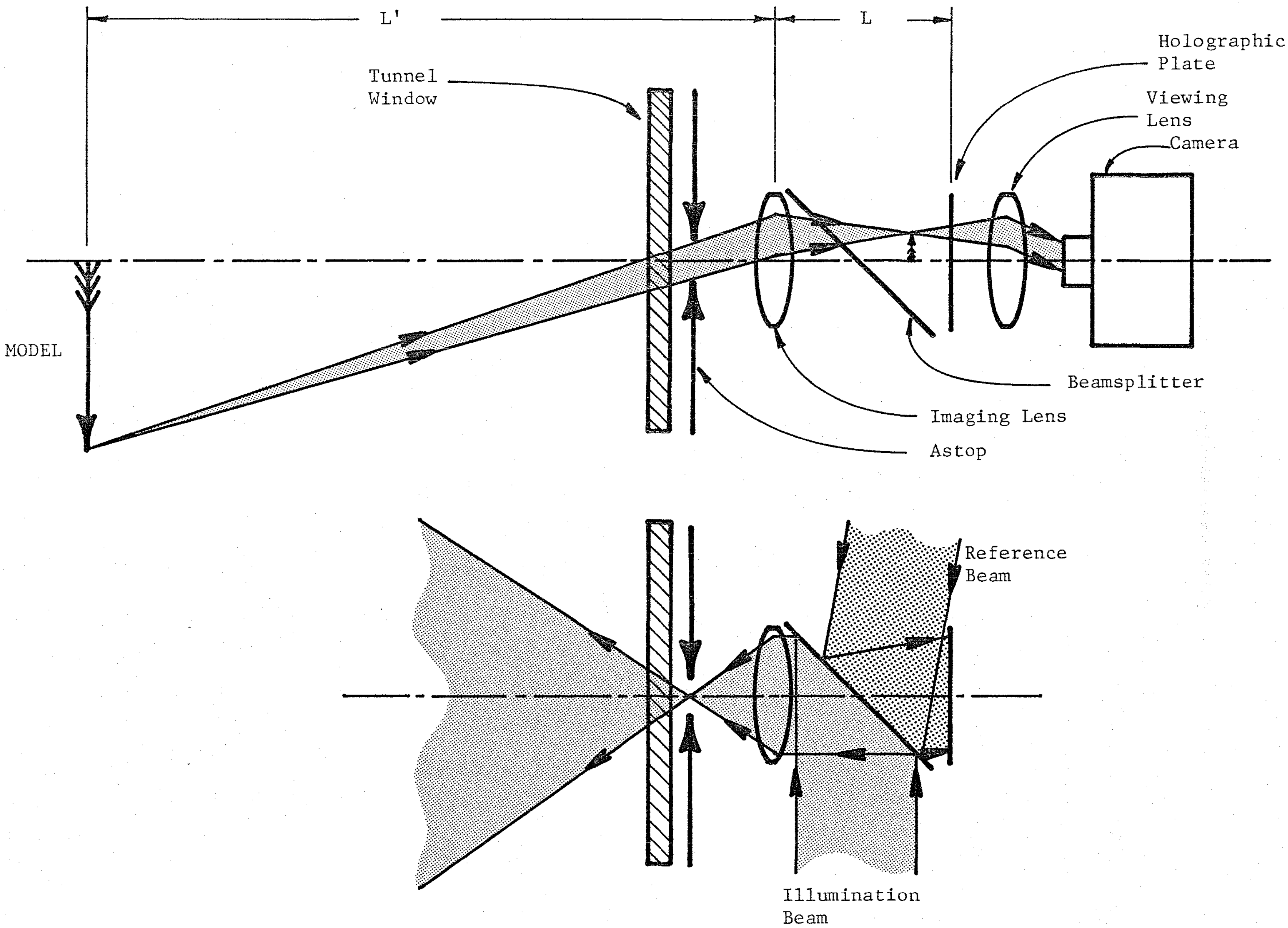

FIGURE 31. A Possible Configuration for 2 Wavelength Holographic Contouring Within the NTF.

After both images have been recorded on the holographic plate, and it has been processed, a continuous wave reference beam is introduced, again via the beamsplitter, for reconstruction. The viewing lens transfers the reconstructed image to a video camera so that it can be monitored from an external location. Note that the aperture of the viewing system is the aperture of the camera lens. And since it is located in the rear focal plane of the viewing lens, the viewing system is telecentric.

For automated remote operation the holographic plate will be a thermoplastic film like Rottenkolber's* HF85. It is characterized by a 50 mm foremat with more than sufficient resolution and instant (10 sec) in-situ processing for a total cycle time of approximately 25 sec. More than 300 exposures can be stored in the device at any given time, and while the unit is overly large (approximately 10x15x60 cm), it has not been configured to save space and could be reduced in size.

Since the depth of focus requirement (± 1/2 meter) is the same for both the holographic and moiré systems, the treatment of Equations 89-95 differs here only by the recording wavelength ($\lambda \cong 0.694\ \mu m$). The slightly modified results are presented here

$$\left.\begin{aligned}
\varepsilon &= 0.5\ \mathrm{m} \\
\lambda &= 0.694\ \mu\mathrm{m} \\
\frac{L'}{D_L} &= 540 \\
L' &= 1.2\ \mathrm{meter} \\
D_L &= 2.2\ \mathrm{mm} \\
D_s &= 0.91\ \mathrm{mm} \\
N_s &= 1100\ \mathrm{spots}\quad .
\end{aligned}\right\} \quad (172)$$

---

* Munich, West Germany

The contour spacing, however, is considerably different, being fully independent of the imaging and reconstruction optics. Reversing the first of Equation 165, a contour spacing of 64 μm requires a wavelength separation on the order of 10 to 40 angstroms (Å) in the visible portion of the spectrum. The multiple wavelengths of argon, keypton, etc., lasers are too widely separated ($\Delta\lambda \cong 250$ Å) and are not usable here. For this reason a tunable dye laser, pumped by a high power pulsed laser, was originally envisioned as the source. However, the conversion efficiency of dye lasers is rather poor, and without further optical amplification there would not be sufficient power to illuminate the large models (~1 meter) anticipated in the NTF. Furthermore, optical amplifiers are narrow band devices, so extraordinary techniques would have to be employed to provide gain at both wavelengths. Such a system (pump laser, dye laser, wide band optical amplifier) would not only be expensive, but prohibitively large. There is some doubt that it could be located in the space available.

One alternative, though, is the ruby laser, which ordinarily oscillates at the R_1 gain peak ($\lambda_1 = 694.3$ nm) of the ruby crystal. There is another peak, however, at the R_2 transition ($\lambda_2 = 692.9$ nm) with sufficient gain for laser oscillation. Wuerker and Heflinger[18] have shown that by tuning the cavity with an etalon, the R_1 transition can be suppressed and R_2 lasing achieved. They used an unstabilized, manually tuned etalon and encountered severe drift that was ultimately the cause of a lack of R_2 lasing repeatability. But consistency in the R_2 transition can be obtained by using an oven stabilized, electronically tuned etalon for wavelength selection. Such a system would have the capability of firing two intense ruby pulses (one at each wavelength) within a few hundred microseconds. There would be more than sufficient power - that of a Q-switched ruby laser - to fully illuminate the model and properly expose the holographic recording material. From the first of Equation 165, the contour spacing would be

$$\Delta a = 172\ \mu\text{m} \tag{173}$$

and with quarter fringe extrapolation, contour resolution to 43 μm should be possible.

Returning to Figure 31 to complete the design, an imaging magnification of

$$m = 20 \tag{174}$$

is required to image the 1 meter model onto the 50 mm thremoplastic film. Therefore,

$$\begin{aligned} L &= L'/m \\ &= 60\ \text{mm} \end{aligned} \tag{175}$$

and from Equations 24, 172, and 175

$$F = 57\ \text{mm} \quad . \tag{176}$$

Finally, combining Equations 169 and 170 produces the restriction

$$\frac{R_{oo}^{\ 2}}{z_o} \leq 4.88\, \frac{\lambda_c^{\ 2}}{\Delta\lambda} \left(\frac{L}{D_L}\right)^2 \quad . \tag{177}$$

Now it is most probable that a Helium Neon laser ($\lambda_c = 0.6328\ \mu\text{m}$) will be used for reconstruction. Using this and Equations 172 and 175 yields

$$\frac{R_{oo}^{\ 2}}{z_o} \leq 1.04\ \text{meter.} \tag{178}$$

Combining this with the last of Equation 157, and recognizing that

$$x_o^{\ 2} + y_o^{\ 2} \leq \left(\frac{\sqrt{2}}{2}\right) 50\ \text{mm} \tag{179}$$

where the term on the right is half of the diagonal of the film, yields a quadratic inequality that can be solved for the dual inequality

$$34 \text{ mm} \le z_o \le 1 \text{ meter} \quad . \tag{180}$$

Now the image of the model in the hologram space is approximately 3 mm thick because of the nonlinear longitudinal magnification characteristic of imaging lenses. It will, therefore, be relatively easy to locate the entire image well within the limits set by Equation 180.

6.0 SUMMARY CONCLUSIONS AND RECOMMENDATIONS

Moiré contouring, scanning heterodyne interferometry, and holographic contouring were examined for their applicability as nonintrusive model deflection sensors within the NTF at NASA's Langley Research Center. The available literature was surveyed, and computations and analysis were performed to establish specific performance requirements, as well as the capabilities and limitations of such a sensor within the geometry of the NTF test section. Also, to gain additional insight into the approach of scanning heterodyne interferometry, the contractor fabricated a limited scale laboratory mock-up of such a system with optical phase locked loop data acquisition.

Based on the foregoing study the following conclusions were drawn:

Moiré Contouring

1) The contour spacing, and hence, deflection accuracy, are indirectly, but ultimately, limited to a few millimeters by the required depth of focus of the model space (1 meter).
2) Extrapolation to fractional contour accuracies is limited to approximately 1/2 mm by the presence of extraneous fringes which are not always spatially separable.
3) Higher accuracies may be obtained by sacrificing depth of focus. But a square law relationship requires a large reduction in depth of focus to obtain a moderate improvement in contour spacing.
4) Planar contours are not possible within the limitations set by the geometry of the NTF test section. In the neighborhood of the model the contours are elliptical in shape.

5) Techniques for removing the troublesome extraneous fringes, such as grid translation, are not applicable because of the vibrations anticipated within the NTF test section.

6) Frame rate is limited only by available video speeds.

Scanning Heterodyne Interferometry

1) The required deflection measurement accuracy necessitates phase measurement accuracies that are near to, or beyond, the state of the art, even for narrow bandwidth laboratory instruments.

2) High sample rates for moderate model coverage (100 samples per raster) aggravate the situation further by demanding even higher bandwidths in such instruments.

3) Phase locked loop data acquisition offers some advantage over open loop phase measurement. But even when ignoring such factors as AM modulation of the returning signal, the requirements are still extreme for such an approach.

4) The transverse resolution is limited by the sample rate, which requires high bandwidths even for moderate model coverage.

Holographic Contouring

1) The contour spacing is independent of any imaging optics used and a function only of the two recording wavelengths. With use of an R_1-R_2 ruby laser, 172 μm contours are possible.

2) There are no troublesome extraneous fringes to limit extrapolation to fractional contour accuracies (43 μm).

3) Planar contours are not possible within the limitations set by the geometry of the NTF test section. Choosing an optical configuration for optimum performance yields well defined parabolic contours.

4) The frame rate is limited to approximately 2 recordings per minute. However, the resultant data will have a resolution of 1100 spots across the field edge.

Of the three techniques examined in this program, holographic contouring appears to offer the most promise. Unlike moiré, it is not hampered by limited contour spacing and extraneous fringes. Furthermore, its transverse resolution can far exceed the limited point sampling resolution of scanning heterodyne interferometry. And finally, the availability of the R_1-R_2 ruby laser as a high power, pulsed, multiple wavelength source makes such a system feasible within the NTF.

To develop a fully operational R_1-R_2 ruby laser holographic contouring system will require an extensive program over a period of approximately three years. If such a program is pursued, the contractor recommends that it be carried out in three phases as follows:

Phase I: Laboratory Breadboard

The tunable ruby laser should be further developed by employing an oven stabilized electronically tuned etalon for dependable operation. A small scale optical system should be fabricated to evaluate the contouring characteristics of the laser. Contour holograms can be made on photographic plates in a stable environment by tuning the laser electronically between flashlamp pulses.

Phase II: On-Site Evaluation

The purpose of Phase II is to extend the development of the Phase I system so that it can be tested at NTF with the tunnel operating at one atmosphere and room temperature. The optical package should be extended to a full scale mock-up and the laser further developed so that both the R_1

and R_2 pulses can be fired within a single flashlamp pulse. Much of the peripheral equipment (such as power supplies and controls) will have to be reshaped and repackaged to fit within the available space in the tunnel. On site, the contour holograms can be recorded on film, changed, developed, and reconstructed manually. Data can be reduced after the tests by the contractor.

Phase III: Prototype Fabrication and Installation

During this final phase of the program, the system of Phase III can be extended to include thermoplastic recording and video monitor of the reconstruction. The entire system will have to be fully automated and repackaged to withstand the extreme environments encountered within the NTF.

REFERENCES

1. P. Beckmann and A. Spizzichino, The Scattering of Electromagnetic Waves from Rough Surfaces, Pergamon, Oxford, (1963).
2. W. D. Bachalo and D. A. Johnson, "Laser Velocimetry and Holographic Interferometry Measurements in Transonic Flows", Presented at the Third International Workshop on Laser Velocimetry, Purdue University, July 11-13, 1978.
3. Lord Rayleigh (Strutt, J. W.), Phil. Mag., Vol. 47, Pg. 193, (1874).
4. T. Merton, J. Phys. Radium, Vol. 13, Pg. 49, (1952).
5. D. M. Meadows, W. O. Johnson, and J. B. Allen, Applied Optics, Vol. 9, Pg. 942, (1970).
6. Warren J. Smith, Modern Optical Engineering: The Design of Optical Systems, McGraw-Hill, New York, (1966).
7. Max Born and Emil Wolf, Principles of Optics, Pergamon, New York, (1970).
8. A. E. Conrady, Applied Optics and Optical Design, Dover, New York, (1957)
9. J. B. Allen and D. M. Meadows, Applied Optics, Vol. 10, Pg. 210, (1971).
10. Ron Bracewell, The Fourier Transform and Its Applications, McGraw-Hill, New York, (1965).
11. Herbert Taub and Donald L. Schilling, Principles of Communication Systems, McGraw-Hill, New York, (1971).
12. Floyd M. Gardner, Phaselock Techniques, 2nd Ed., John Wiley, New York, (1979).

13. Howard M. Berlin, *Design of Phase-Locked Loop Circuits, With Experiments*, Howard W. Sams, Indianapolis, (1978).

14. Charles M. Vest, *Holographic Interferometry*, John Wiley, New York, (1979).

15. B. P. Hildebrand, "A General Analysis of Contour Holography", Ph.D. Dissertation, University of Michigan, (1967).

16. Joseph W. Goodman, *Introduction to Fourier Optics*, McGraw-Hill, New York, (1968).

17. J. R. Varner, "Multiple Frequency Holographic Controuring," Ph.D. Dissertation, University of Michigan, (1971).

18. R. F. Wuerker and L. D. Heflinger, "Ruby Laser R_1-R_2 Contouring", presented to the Conference and exhibition on the Engineering Uses of Coherent Optics, University of Strathclyde, Glasgow, Scotland, April, (1975).

1. Report No.
NASA CR-165853

2. Government Accession No.

3. Recipient's Catalog No.

4. Title and Subtitle
"A Study of Model Deflection Measurement Techniques Applicable Within the National Transonic Facility"

5. Report Date
February, 1982

6. Performing Organization Code

7. Author(s)
B. P. Hildebrand and J. L. Doty

8. Performing Organization Report No.
81-2189-10F

9. Performing Organization Name and Address
Spectron Development Laboratories, Inc.
3303 Harbor Blvd., Suite G-3
Costa Mesa, Ca. 92626

10. Work Unit No.

11. Contract or Grant No.
NAS1-16564

12. Sponsoring Agency Name and Address
National Aeronautics and Space Administration
Washington, DC 20546

13. Type of Report and Period Covered
Contractor Report

14. Sponsoring Agency Code

15. Supplementary Notes
Langley technical monitor: H. K. Holmes
Final Report

16. Abstract

A study was conducted to establish specific performance requirements and goals for a model deflection sensor to be installed in the National Transonic Facility (NTF) presently under construction at NASA's Langley Research Center. The system as envisioned will be nonintrusive, and have the capability of mapping or contouring the surface of a 1 x 1 meter model with a resolution of 50 to 100 points.

Three distinct concepts - moiré contouring, scanning interferometry and holographic contouring - were examined in detail for their practicality and potential to meet the above requirements. A review of the literature was conducted and extended by theoretical analysis to determine the capabilities and limitations of each concept within the constraints set by the geometry of the NTF test section.

The results of this program provide a solid understanding of the limitations of each of the three techniques as they apply within the geometry of the NTF.

17. Key Words (Suggested by Author(s))
Model Deflection Sensor,
Moiré, Holographic Contouring,
Scanning Interferometry

18. Distribution Statement
Unclassified-Unlimited

19. Security Classif. (of this report)
Unclassified

20. Security Classif. (of this page)
Unclassified

21. No. of Pages
97

22. Price

N-305

End of Document